

# UC Berkeley

## UC Berkeley Previously Published Works

### Title

Aerobic respiration controls on shale weathering

### Permalink

<https://escholarship.org/uc/item/4mx247ng>

### Authors

Stolze, Lucien

Arora, Bhavna

Dwivedi, Dipankar

et al.

### Publication Date

2023

### DOI

10.1016/j.gca.2022.11.002

### Copyright Information

This work is made available under the terms of a Creative Commons Attribution-NonCommercial-NoDerivatives License, available at

<https://creativecommons.org/licenses/by-nc-nd/4.0/>

Peer reviewed



Contents lists available at ScienceDirect

# Geochimica et Cosmochimica Acta

journal homepage: [www.elsevier.com/locate/gca](http://www.elsevier.com/locate/gca)



## Aerobic respiration controls on shale weathering

Lucien Stolze<sup>a,\*</sup>, Bhavna Arora<sup>a</sup>, Dipankar Dwivedi<sup>a</sup>, Carl Steefel<sup>a</sup>, Zhi Li<sup>a,b</sup>, Sergio Carrero<sup>a,c</sup>, Benjamin Gilbert<sup>a</sup>, Peter Nico<sup>a</sup>, Markus Bill<sup>a</sup>

<sup>a</sup> Earth and Environmental Sciences Area, Lawrence Berkeley National Laboratory, Berkeley, CA 94720, USA

<sup>b</sup> College of Civil Engineering, Tongji University, Shanghai 200092, China

<sup>c</sup> Institute of Environmental Assessment and Water Research, Barcelona 08034, Spain



### ARTICLE INFO

#### Article history:

Received 16 May 2022

Accepted 6 November 2022

Available online 9 November 2022

#### Keywords:

Shale weathering

Aerobic respiration

Multiphase transport

Carbon cycling

Reactive transport modeling

### ABSTRACT

The weathering of shale exerts an important control on the hydrochemical fluxes to river systems, thus influencing the global carbon, nutrient, and geochemical cycles. However, the quantitative understanding of shale weathering and its impact on global biogeochemical cycles remains inadequate due to the complex interplay between hydrological, biogeochemical, and physical processes. In this study, we develop a novel modeling approach to quantitatively interpret the long-term chemical weathering of shale occurring since the last glaciation period (15,000 years) leading to the present geochemical conditions. The model explicitly considers processes occurring across multiple phases and involved in the weathering, including: (i) the infiltration of meteoric water, (ii) the interactions between the water and the mineral assemblage via dissolution/precipitation reactions, (iii) the microbially-mediated oxidation of organic matter, (iv) the evolution of porosity induced by mineral reactions, and (v) the exchange of gases between the subsurface and the atmosphere. To implement and test our model, we conduct this study at a well-instrumented hillslope underlain by Mancos Shale and located at the East River study site, Western Colorado. Consistent with field observations, the model successfully reproduces the stratified weathering front, the complex spatial distribution of organic carbon, and the gaseous emissions of carbon dioxide from the subsurface. Model simulations show that aerobic respiration exerts a fundamental control on the weathering of shale. While previous studies have highlighted the diffusion of oxygen from the atmosphere as the primary mechanism for shale weathering, our model simulations demonstrate that aerobic respiration limits the propagation of oxygen in the shallow subsurface, and thereby inhibits the dissolution of pyrite at depth. Aerobic respiration is particularly favored in the top soil horizon due to the constant flux of oxygen from the atmosphere, the replenishment of fresh litter/plant-derived organic matter, and to a lesser extent the presence of fossil shale-associated organic matter. The acidic pore water generated through aerobic respiration within the shallow subsurface is transported to greater depths, where it sustains the dissolution of carbonate (dolomite in this example). Overall, our results demonstrate that the evolution of pyrite and carbonate depletion fronts are significantly different, and primarily depend on the ability of microorganisms to carry out microbial respiration and the various transport pathways of reactants controlling the mineral reactions under partially saturated conditions.

© 2022 The Authors. Published by Elsevier Ltd. This is an open access article under the CC BY-NC-ND license (<http://creativecommons.org/licenses/by-nc-nd/4.0/>).

### 1. Introduction

Chemical weathering consists of the conversion of protolith into regolith, and contributes to the global cycle of carbon and nitrogen (Houlton et al., 2018), the formation of biologically active soil and the evolution of landscape (Hunt et al., 2021). In particular, this critical zone process determines the hydrological properties of aquifers (Navarre-Sitchler et al., 2015; Gu et al., 2020a), the sea-

sonal variation in hydrochemical exports to rivers (Maher, 2011; Ameli et al., 2017; Newcomer et al., 2021; Stewart et al., 2021), and the mobilization of trace elements and contaminants (Tuttle et al., 2009; Morrison et al., 2012). Weathering of shale sedimentary rock is particularly important since shale accounts for 25 % of Earth's continental rocks (Amiotte-Suchet et al., 2003) and represents a large reservoir of carbon and nitrogen given its high levels of fossil organic matter (OM) and carbonate minerals (Petsch et al., 2005; Copard et al., 2007; Jin et al., 2014; Fox et al., 2020).

\* Corresponding author.

E-mail address: [lstolze@lbl.gov](mailto:lstolze@lbl.gov) (L. Stolze).

A significant challenge in understanding the mechanisms controlling the dynamics and extent of weathering lies in the complex interplay between various physical, chemical, and biological processes occurring within multiple phases. In particular, the continuous diffusion of atmospheric gases and the infiltration of meteoritic water into the subsurface modify the composition of the pore water, influence the biogeochemical reactions, and lead to concentration gradients (Maher et al., 2009; White et al., 2009; Arora et al., 2016; Yabusaki et al., 2017). While the ingress of oxygen is known to trigger the oxidative dissolution of pyrite (Manning et al., 2013; Battistel et al., 2019; Ahmadi et al., 2022), the primary drivers for the dissolution of carbonate and silicate minerals remain unclear as multiple processes such as microbial respiration and sulfide dissolution can acidify the pore water (e.g., Beaulieu et al., 2011; Jin et al., 2013; Bao et al., 2017; Tremosa et al., 2020; Gu et al., 2020b). Quantifying the contribution of these mechanisms is particularly difficult as various pools of organic matter with different reactivity and bioavailability might coexist in shale formation (Fox et al., 2020). For example, fossil organic matter associated with shale can be consumed through aerobic respiration when exposed to the atmosphere (Petsch et al., 2005; Jin et al., 2013). In addition, modern organic matter derived from litter/plant sources can be transported to depth, sorb onto solid materials, and/or sustain microbially-mediated reactions (Dwivedi et al., 2017, 2019; Chapelle, 2021). Furthermore, the extent and dynamics of the biogeochemical reactions are intimately linked to the gas and hydrochemical fluxes. Such fluxes are in turn controlled by the degree of water saturation and fluid residence time, the intrinsic properties of the bedrock (i.e., porosity and permeability), and the degree of weathering (Jin et al., 2011; Navarre-Sitchler et al., 2015; Lebedeva and Brantley, 2020; Gu et al., 2020a).

Given this complexity, understanding the primary drivers of weathering can benefit from reactive transport modeling that is instrumental to quantitatively interpret the tight coupling between physical, chemical, and biological processes in porous media (Steeffel, et al., 2005; Steeffel et al., 2015; Li et al., 2017; Dwivedi et al., 2018a; Steeffel, 2019; Maher and Navarre-Sitchler, 2019; Stolze et al., 2019a, 2019b; Cogorno et al., 2022). In this regard, remarkable applications of numerical models to explore chemical weathering include the optimization of the disposal of waste rock (Tremosa et al., 2020; Muniruzzaman et al., 2021), the characterization of the porosity and mineral surfaces evolution at microscopic scale (Navarre-Sitchler et al., 2011), and the interpretation of seasonal chemical exports at catchment scales (Godderis et al., 2006; Beaulieu, et al., 2011). To date, only a few studies have analyzed the evolution of weathering front under natural conditions and over millennial time scales using process-based reactive transport models (Bolton et al., 2006; Maher et al., 2009; Heidari et al., 2017; Bao et al., 2017). Although these studies have offered valuable insights into deep time weathering and its control on the hydrogeochemical conditions, none of the modeling efforts have yet explicitly accounted for microbially-mediated reactions and the presence of different sources of organic matter (i.e., fresh litter/plant-derived and/or shale-associated). This shortcoming limits the rigorous assessment of shale weathering mechanisms, and, in particular the evaluation of the role of aerobic respiration in the loss of fossil organic matter as well as the dissolution of sulfide and carbonate minerals (Littke et al., 1991; Petsch, et al., 2000; Jin et al., 2014).

To address these gaps, this study investigates the weathering of shale over a hillslope-to-floodplain transect located at the East River study site, a pristine mountainous watershed of Western Colorado, USA (Hubbard et al., 2018; Tokunaga et al., 2019). At this site, field investigations have shown a complex stratified weathering front of pyrite and dolomite associated with the local Mancos

shale environment. We implement a reactive transport model based on an updated version of CrunchTope (Steeffel et al., 2015) that includes partially saturated flow (Li et al., 2021), thus providing an opportunity to analyze the coupling between hydrochemical transport, gas exchange at the soil/atmosphere interface, microbial respiration, and the weathering of shale. The model development is constrained by the field dataset that includes the aqueous, gas, and solid phases. The specific objectives of this study are to identify the key biogeochemical and physical processes controlling the long-term dissolution of the primary minerals and to assess the relative contribution of the various pools of organic matter on weathering (shale and fresh-litter/plant-derived).

## 2. Field site description and dataset collection

The hillslope-to-floodplain transect considered in this study is located in the East River watershed of the Upper Colorado River basin encompassing the Rocky Mountain Biological Laboratory (Fig. 1). The transect is 140 m long with an average slope of 19 %, exposed northeast and drains into an adjacent floodplain. The altitude of the hillslope transect ranges between 2750 m and 2800 m. The shallow soil profiles (i.e., 1 m ± 0.3 thick; Wan et al., 2021) are vegetated with grasses, forbs, and shrubs representative of the regional lower montane life zone. The transect is underlain by Cretaceous Mancos shale that is broadly distributed throughout the southwestern United States and has been shown to strongly control the aqueous chemistry and seasonal hydrochemical exports to the river through weathering (Morrison et al., 2012; Tokunaga et al., 2019; Arora et al., 2021).

The climate at the field site is continental, subarctic characterized by long cold winters and short cool summers with average, minimum and maximum temperature of 3 °C, −9.2 °C, and 9.8 °C, respectively. The average annual precipitation and evapotranspiration (ET) are ~ 700 ± 100 mm and ~ 300 mm, respectively with about 70 % of the precipitation occurring as snow fall between October and May (Carroll et al., 2018). The months of November to April are characterized by persistent snow cover and are followed by a warming-driven snowmelt and rapid increase in ET. Summer months are characterized by an arid climate and intermittent monsoonal rain events, which do not significantly impact the net recharge due to the strong ET during this period. The water table rises abruptly during snowmelt, starting end of April, and then progressively declines over the year (Wan et al., 2021; Dwivedi et al., 2022). Surface runoff and/or perched water table have not been observed at the site.

The study site and instrumentation installed over the transect to monitor the vadose zone and the groundwater have been described elsewhere (Hubbard et al., 2018; Tokunaga et al., 2019; Wan et al., 2021). For completeness, a brief description is provided here. In 2016, three observation wells (PLM1, PLM2, and PLM3; Fig. 1) were drilled to a depth of 10 m using a track-mounted drill rig and a 0.14 m diameter ODEX drilling bit. The wells were equipped with suction lysimeters to carry-out vertically-discrete pore water sampling; pressure transducers to perform daily-measurements of the water table (AquaTROLL 2000; except in PLM2 where the water table was determined from equilibrium pressure and moisture measurements; Wan et al., 2021); and temperature sensors.

### 2.1. Solid phase composition

Multi-depth solid sampling and analyses were performed to assess the mineralogy and spatial distribution of carbon in the subsurface. In particular, mineral concentrations in PLM1 and PLM2 were determined from X-ray diffraction (XRD) measurements

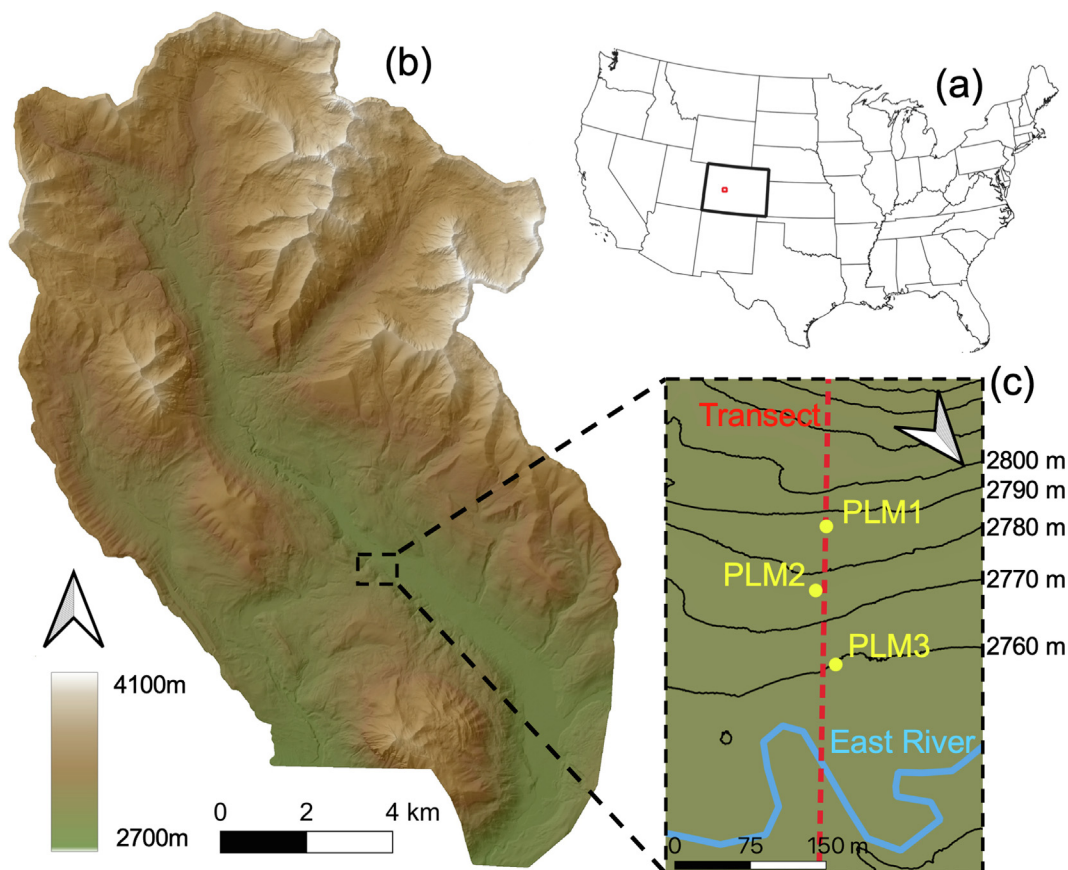


**Fig. 1.** Location of the East River Watershed study area (a) and topographic map showing the 140 m long hillslope transect in the Rocky Mountains and the locations of the three monitoring wells separated by ~ 70 m from each other (b-c).

performed on samples collected during installation of the monitoring wells (Wan et al., 2021). Additional XRD measurements were performed on sub-core samples collected in PLM3 at approximately 0.3 m intervals between the upper part of the core and 10 m below ground surface (this study). These samples were powdered in an agate mortar and stored in a glovebox under  $N_2$  conditions to avoid mineral oxidation between sample preparation and analysis. The XRD analyses were performed using a Rigaku SmartLab high-resolution XRD diffractometer with a Bragg-Brentano geometry. The diffractometer was equipped with a theta-theta goniometer and a rotating sample holder using  $Cu$  ( $\lambda k\alpha_1 = 1.5406 \text{ \AA}$  and  $\lambda k\alpha_2 = 1.5444 \text{ \AA}$ ) cathode. For clay identification, an aliquot from the  $< 2 \mu\text{m}$  particle size suspension was dropped on a zero-background plate and dried at room temperature to obtain oriented clay samples, whereas the bulk ground rock samples were placed in an aluminum holder to ensure random particle orientations. Bulk rock samples were collected from  $2$  to  $90^\circ 2\theta$  with a  $0.02^\circ 2\theta$  step-size and count times of  $2 \text{ s}$  per step. Oriented clay sample was measured ( $3$  to  $25$  and  $3$  to  $75^\circ 2\theta$  with  $0.02^\circ 2\theta$  step-size and  $10$  and  $2 \text{ s}$  per step, respectively) under four different conditions: (1) dry at room temperature, (2) saturated with ethylene-glycol and heated at  $333 \text{ K}$  for  $1 \text{ h}$ , (3) heated at  $673 \text{ K}$  for  $1 \text{ h}$ , and (4) heated at  $823 \text{ K}$  for  $1 \text{ h}$ . The diffraction patterns were analyzed using the software Match (Putz and Branderburg, 2011) and the PDF-2 mineral database (Gaste-Rector and Blanton, 2019). The mineral concentrations were quantified with the Rietveld refinement method using the software Rockjock (Eberl, 2003). Illite, muscovite, and chlorite were identified in all samples and presence of smectite was detected in the upper  $30 \text{ cm}$  of PLM3

(Supplementary data). Illite, muscovite, and smectite were represented with a single phase in the model considering the similar structural properties of illite and muscovite and the uncertainty on smectite concentration quantification.

Table 1 presents the mass fractions, volume fractions and bulk surface areas of the minerals composing the parent shale rock as defined in the model. The mass fractions were calculated as the average of XRD measurements performed on unaltered samples collected below the weathering front in PLM3 (i.e., greater than  $4 \text{ m}$  bgs). The bedrock primarily consists of quartz ( $40.22 \text{ wt\%}$ ) and clay minerals ( $36.3 \text{ wt\%}$  in total) composed of chlorite and illite. The dominant carbonate mineral is dolomite ( $13.70 \text{ wt\%}$ ) and small amounts of calcite were detected ( $1.23 \text{ wt\%}$ ). Pyrite and shale-associated organic carbon represents minor fractions of the mineral assemblage ( $0.90 \text{ wt\%}$  and  $1.25 \text{ wt\%}$ , respectively). Iron oxides were not detected below the weathering front. Mineral concentrations in PLM1 and PLM2 from Wan et al. (2021) were normalized based on the parent rock mineral composition measured in PLM3. Total organic carbon content (TOC) was determined from solid samples collected during installation of the monitoring wells at depth intervals of  $10 \text{ cm}$  above  $1 \text{ m}$  bgs and  $\sim 90 \text{ cm}$  below  $1 \text{ m}$  bgs. TOC analysis was performed using a carbon analyzer (Shimadzu TOC-VCSH; Wan et al., 2019).

## 2.2. Soil gas and groundwater composition

Aqueous-phase sampling and analyses were carried out between  $0.2 \text{ m}$  and  $8 \text{ m}$  bgs from the suction lysimeters installed in the three monitoring wells and at weekly to monthly time inter-

**Table 1**

Mass fractions, volume fractions, and bulk surface areas of the minerals composing the shale bedrock as defined in the model.

	Dolomite	Albite	Quartz	Chlorite	Illite	Calcite	Pyrite	Goethite	Shale OC
Molar volume, $V_m$ [cm <sup>3</sup> /mol]	64.37	100.25	22.69	215.88	140.67	36.93	23.94	20.82	15 <sup>(a)</sup>
Molar mass, $M_m$ [g/mol]	184.40	262.22	60.08	713.51	400.10	100.09	119.98	88.85	12
Mass fraction, $w_m$ [wt%]	13.70	6.69	40.22	4.30	32.00	1.20	0.90	0.00	1.25
Volume fraction, $\theta_{m,o}$ [%]	12.6	6.74	40.02	4.23	29.65	1.17	0.47	0.00	4.12
Specific surface area, $A_{m,s}$ [m <sup>2</sup> /g]	1.82 <sup>(b)</sup>	0.10 <sup>(c)</sup>	0.01 <sup>(d)</sup>	1.1 <sup>(e)</sup>	42 <sup>(f)</sup>	0.22 <sup>(g)</sup>	0.05 <sup>(h)</sup>	-*	-
Bulk surface area, $A_{m,o}$ [m <sup>2</sup> /m <sup>3</sup> ]	1069	29	17	250	57,601	11	1.9	-	1**

<sup>(a)</sup> Bao et al. (2017); <sup>(b)</sup> Marouf et al. (2009); <sup>(c)</sup> Moore et al. (2019); <sup>(d)</sup> Stolze et al. (2020); <sup>(e)</sup> Brandt et al. (2003); <sup>(f)</sup> Bibi et al. (2011); <sup>(g)</sup> Sø et al. (2012); <sup>(h)</sup> Williamson and Rimstidt (1994); \*initially not present; \*\*assumed.

vals from fall 2016 to fall 2019 (Wan et al., 2019). Major cations and trace elements were determined from filtered HNO<sub>3</sub>-acidified samples with inductively coupled plasma mass spectrometry (ThermoFischer, MA, USA). Anions were measured from unacidified samples using ion chromatography (ICS-2100, Dionex, CA, USA). Dissolved carbon was measured using a TOC-VCPH analyzer (Shimadzu Corporation, Japan). In particular, dissolved organic carbon (DOC) was measured as non-purgeable organic carbon (NPOC) by purging acidified samples with carbon-free air to remove DIC. DIC was calculated by subtracting the DOC to the total measured dissolved carbon. Major cations concentrations and pH measurements show that the groundwater is of Ca-Mg-SO<sub>4</sub> and Na-SO<sub>4</sub> types and has a neutral to slightly basic pH (i.e., [6.67; 8.63]) reflecting the local geochemical conditions with dolomite, pyrite, and albite dominating the reactive part of the mineral assemblage.

Gas samples were collected in the vicinity of PLM2 with a peristaltic pump from pre-installed lysimeters at 25 cm, 91 cm, and 152 cm bgs. Supplementary samples were collected by introducing a ¼ inch diameter tubing into the soil. After purging the sampling tubes and well lysimeters, the samples were collected in 60-mL glass, gas tight syringes and stored in pre-evacuated 60-mL serum bottles stoppered with 20-mm diameter blue chlorobutyl septa (Bellco Glass, Inc., Vineland, NJ). CO<sub>2</sub> and CH<sub>4</sub> concentrations were determined with a GC-2014 Shimadzu gas chromatograph (GC-2014 Shimadzu, Kyoto, Japan). ~ 4.5 mL of gas was injected into a 1 mL stainless steel loop. CO<sub>2</sub> and CH<sub>4</sub> were separated on a packed HayeSep-D packed column (4 m × 1/8 in.). CO<sub>2</sub> was reduced to CH<sub>4</sub> in a methanizer. Both reduced CO<sub>2</sub> and CH<sub>4</sub> were quantified with a flame ionization detector (FID).

### 3. Modeling approach

Shale weathering was simulated over a period of 15,000 years (i.e., starting from the last glaciation period; Quirk et al., 2022) with explicit consideration for the impact of external forcing (i.e., meteoric water infiltration and atmospheric gases ingress), unsaturated flow and multiphase transport (gas and water), microbially-mediated reactions, water-rock reactions, and the different pools of organic matter (i.e., modern fresh litter/plant-derived and fossil shale-associated).

#### 3.1. Reaction network

The model considers a series of kinetically-controlled microbially-mediated and geochemical reactions. The reactions are controlled by the continuous supply of aqueous species and fresh organic matter transported with the infiltrating meteoric water, the ingress of atmospheric gases into the subsurface, and the presence of fossil mineral-associated organic matter. A visual illustration of the conceptual framework for the proposed modeling approach is shown in Fig. 2.

The reaction network is composed of (i) the microbially-mediated aerobic oxidation of dissolved organic matter (DOM), (ii) the oxidative dissolution of the sulfide mineral pyrite induced

by oxygen and ferric iron, (iii) the oxidation of ferrous iron to ferric iron and the precipitation of iron oxide, and (iv) the dissolution/precipitation of carbonate, silicate, and clay minerals. The set of kinetically-controlled reactions is shown in Table 2.

Based on recent studies characterizing the sediment organic matter in the East River mountainous watershed (Fox et al., 2020), two distinct types of reactive organic matter were considered: a fresh litter/plant-derived organic matter present at the soil surface and a fossil shale-associated organic matter initially present in the bedrock. The sorption of fresh organic matter onto aquifer materials (Chapelle, 2021) as well as the release of DOM from shale-associated organic matter (Schillawski and Petsch, 2008) were defined as first-order mass-transfer processes (Dwivedi et al., 2017, 2018b; Rogers et al., 2021) controlled by the rate expression:

$$R_{DOM} = k_{DOM} A_{SOM} \left( 1 - \frac{C_{DOM}}{K_{eq,DOM}} \right) \quad (1)$$

where  $k_{DOM}$  [mol/m<sup>2</sup>/s] is the rate constant,  $A_{SOM}$  is the exposed surface area of the solid organic matter (SOM) [m<sup>2</sup>], and  $C_{DOM}$  and  $K_{eq,DOM}$  are the DOM concentration and the equilibrium controlling the reaction, respectively.

The co-occurring presence of DOM and oxygen sustains the aerobic respiration (Van Capellen and Wang, 1995; Regnier and Steefel, 1999). The rate controlling this biotic reaction was expressed with a Michaelis-Menten rate equation (Van Capellen and Gaillard, 1996):

$$R_S = \mu_{max,S} \frac{C_S}{K_{m,S} + C_S} \frac{C_{TEA}}{K_{m,TEA} + C_{TEA}} \quad (2)$$

where  $\mu_{max,S}$  is the maximum rate of reaction for the substrate denoted  $S$  [mol/L/s].  $C_S$  and  $K_{m,S}$  are the concentration and half-reaction constant of the substrate, respectively,  $C_{TEA}$  and  $K_{m,TEA}$  are the concentration and half-reaction constant of the electron acceptor [mol/L], respectively.

The abiotic transformation of the mineral assemblage involves the dissolution of the primary minerals and the precipitation of secondary minerals. These dissolution/precipitation reactions were controlled by rate expressions accounting for thermodynamic constraints, the local hydrochemical conditions, and the exposed surface area of the minerals. In particular, the dissolution/precipitation of silicate, carbonate, and clay minerals were controlled by parallel rates based on the transition state theory to account for the effect of pH (Helgeson et al., 1984; Lasaga, 1984; Lasaga, 1998; Palandri and Kharaka, 2004; Steefel et al., 2015):

$$R_m = A_m \left( \begin{array}{l} k_{m,H_2O} \exp\left(\frac{-E_{a,m,H_2O}}{RT}\right) + \\ k_{m,H^+} [H^+]^{x_{1,m}} \exp\left(\frac{-E_{a,m,H^+}}{RT}\right) + \\ k_{m,OH^-} [OH^-]^{x_{2,m}} \exp\left(\frac{-E_{a,m,OH^-}}{RT}\right) \end{array} \right) \left( 1 - \frac{IAP_m}{K_{eq,m}} \right) \quad (3)$$

where  $A_m$  is the total exposed surface area of the mineral  $m$  [m<sup>2</sup>],  $k_{m,H_2O}$ ,  $k_{m,H^+}$ , and  $k_{m,OH^-}$  are the effective rate constants for the

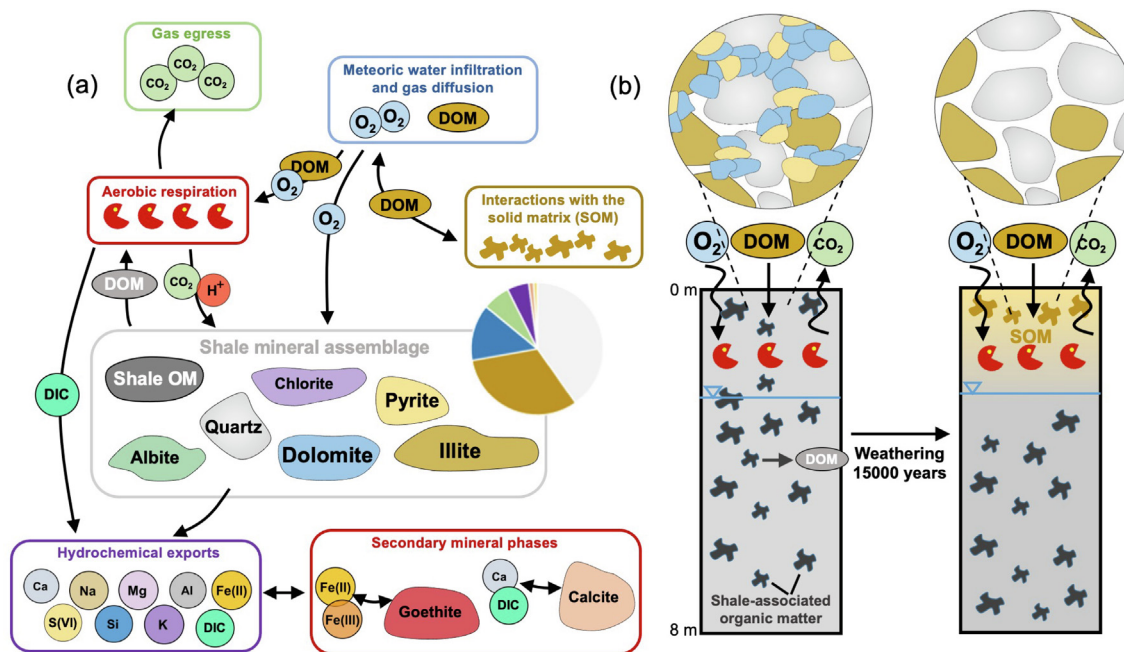


**Fig. 2.** Illustration of the conceptual framework used to simulate the weathering of shale: (a) reaction network and (b) conceptual model; the color-coded pie chart shown with the shale mineral assemblage in (a) illustrates the mass fraction of the minerals composing the parent bedrock.

**Table 2**

Kinetic aqueous reactions and solid mineral phase dissolution/precipitation reactions included in the model. The reactions involving DOM, defined with the general stoichiometry  $\text{CH}_2\text{O}$ , were included for both litter-derived and shale-associated organic matter.

Aqueous reactions	
Processes	Reaction stoichiometry
Aerobic respiration	$\text{CH}_2\text{O} + \text{O}_2 = \text{H}^+ + \text{HCO}_3^-$
Ferrous iron oxidation	$\text{Fe}^{2+} + 0.25\text{O}_2 + \text{H}^+ = \text{Fe}^{3+} + 0.5\text{H}_2\text{O}$
Mineral phase dissolution/precipitation reactions	
Minerals	Reaction stoichiometry
Dolomite	$\text{MgCa}(\text{CO}_3)_2 + 2\text{H}^+ = \text{Mg}^{2+} + \text{Ca}^{2+} + 2\text{HCO}_3^-$
Albite	$\text{NaAlSi}_3\text{O}_8 + 4\text{H}^+ + 4\text{H}_2\text{O} = \text{Al}^{3+} + \text{Na}^+ + 3\text{H}_4\text{SiO}_4$
Chlorite*	$\text{Fe}_5\text{Al}_2\text{Si}_3\text{O}_{10}(\text{OH})_8 + 16\text{H}^+ = 5\text{Fe}^{2+} + 2\text{Al}^{3+} + 3\text{H}_4\text{SiO}_4 + 6\text{H}_2\text{O}$
Quartz	$\text{SiO}_2 + 2\text{H}_2\text{O} = \text{H}_4\text{SiO}_4$
Pyrite (oxygen)	$\text{FeS}_2 + 3.5\text{O}_2 + \text{H}_2\text{O} = \text{Fe}^{2+} + 2\text{SO}_4^{2-} + 2\text{H}^+$
Pyrite (ferric iron)	$\text{FeS}_2 + 14\text{Fe}^{3+} + 8\text{H}_2\text{O} = 15\text{Fe}^{2+} + 2\text{SO}_4^{2-} + 16\text{H}^+$
Goethite	$\text{Fe}^{3+} + 2\text{H}_2\text{O} = \text{FeOOH} + 3\text{H}^+$
Calcite	$\text{Ca}^{2+} + \text{CO}_3^{2-} = \text{CaCO}_3$
Illite**	$2.35\text{Al}^{3+} + 3.4\text{H}_4\text{SiO}_4 + 0.85\text{K}^+ + 0.25\text{Fe}^{2+} = \text{K}_{0.85}\text{Al}_{2.35}\text{Fe}_{0.25}\text{Si}_{3.4}\text{O}_{10}(\text{OH})_2 + 8.4\text{H}^+ + 1.6\text{H}_2\text{O}$
SOM	$\text{SOM} = \text{CH}_2\text{O}$

\* The stoichiometry of chamosite was adopted based on the XRD analyses showing a  $\text{Fe}^{2+}$ -rich chlorite.

\*\* The stoichiometry provided in Godderis et al. (2006) was adopted based on the XRD analyses showing a  $\text{Al}^{3+}$ -rich illite.

reaction accounting for its dependency to water, protons and hydroxide at 25 °C [ $\text{mol}/\text{m}^2/\text{s}$ ],  $E_{a,m, \text{H}_2\text{O}}$ ,  $E_{a,m, \text{H}^+}$ , and  $E_{a,m, \text{OH}^-}$  are the respective activation energy [ $\text{cal}/\text{mol}$ ] to account for the temperature dependency of the reaction using the Arrhenius relationship,  $R$  is the gas constant (1.9872 cal/K/mol),  $T$  is the absolute temperature [K],  $IAP_m$  and  $K_{eq,m}$  are the ion activity product [-] and equilibrium constant [-] of the reaction, respectively. The quantities in brackets (e.g.,  $[\text{H}^+]$ ,  $[\text{OH}^-]$ ) represent the molar concentration of dissolved species.

Considering the constant ingress of oxygen from the atmosphere and the pristine conditions at the hillslope (i.e., circumneutral pH and low nitrogen concentrations), the oxidative dissolution of pyrite was assumed abiotic. As shown in Table 2, we defined two distinct reactions of pyrite with oxygen and ferric iron (McKibben and Barnes, 1986; Moses et al., 1987; Williamson and Rimstidt,

1994). These reactions were respectively controlled by the empirical rate formulations developed for pyrite (Williamson and Rimstidt, 1994) as:

$$R_{\text{pyr}, \text{O}_2} = k_{\text{pyr}, \text{O}_2} A_{\text{pyr}} [\text{O}_2]^{x_{\text{pyr},1}} [\text{H}^+]^{x_{\text{pyr},2}} \quad (4)$$

and

$$R_{\text{pyr}, \text{Fe}^{3+}} = k_{\text{pyr}, \text{Fe}^{3+}} A_{\text{pyr}} [\text{Fe}^{3+}]^{x_{\text{pyr},3}} [\text{Fe}^{2+}]^{x_{\text{pyr},4}} [\text{H}^+]^{x_{\text{pyr},5}} \quad (5)$$

where  $k_{\text{pyr}, \text{O}_2}$  and  $k_{\text{pyr}, \text{Fe}^{3+}}$  are the rate constants [ $\text{mol}/\text{m}^2/\text{s}$ ],  $A_{\text{pyr}}$  is the total exposed surface area of pyrite [ $\text{m}^2$ ],  $x_{\text{pyr},1}$ ,  $x_{\text{pyr},2}$ ,  $x_{\text{pyr},3}$ , and  $x_{\text{pyr},4}$  [-] are exponents.

The initial bulk surface areas of the reactive minerals ( $A_{m,0}$ , Table 1) were defined by considering the volume fractions of the minerals and their specific surface areas (i.e., literature values

shown in Table 1), and by accounting for the lower reactivity of minerals composing the shale. This effect has been attributed to the low pore connectivity of the bedrock (Pandey and Rajaram, 2016), the presence of surface coatings (Battistel et al., 2021; Stolze et al., 2022), and/or the larger size of the natural solid entities in comparison to the particulate size typically used for laboratory BET surface measurements (Heidari et al., 2017; Navarre-Sitchler et al., 2011). Therefore, we reduced the bulk surface area by applying a scaling factor  $S_f$  determined from a previous study characterizing mineral weathering rates (i.e.,  $1.61 \times 10^{-3}$ , Navarre-Sitchler et al., 2011). The initial bulk surface area of mineral  $m$  was calculated as:

$$A_{m,0} = S_f \frac{A_{m,s} M_m}{V_m} \theta_{m,0} \quad (6)$$

where  $A_{m,s}$ ,  $M_m$ ,  $V_m$ , and  $V_{m,f}$  are the specific surface area [ $\text{m}^2/\text{g}$ ], molar mass [ $\text{g}/\text{mol}$ ], molar volume [ $\text{m}^3/\text{mol}$ ], and volume fraction of mineral  $m$ , respectively.

Furthermore, the model considers the oxidation of ferrous iron, generated by the dissolution of pyrite and illite, to ferrous iron upon reaction with dissolved oxygen. The reaction was kinetically controlled by the general rate law (Stumm and Morgan, 1961; Singer and Stumm, 1970; Haberer et al., 2015):

$$R_{\text{Fe}} = k_{\text{Fe}} [\text{Fe}^{2+}] [\text{O}_2] [\text{H}^+]^{-2} \quad (7)$$

where  $k_{\text{Fe}}$  is the rate constant [ $\text{mol}/\text{s}$ ].

The subsequent precipitation of ferrous iron into an iron oxide mineral phase was expressed as a function of the degree of oversaturation and goethite was defined as the representative type of iron oxide based on the XRD analyses:

$$R_{\text{goe}} = k_{\text{goe}} \left( 1 - \frac{IAP_{\text{goe}}}{K_{\text{eq, goe}}} \right) \exp \left( \frac{-E_{a,\text{goe}}}{RT} \right) \quad (8)$$

where  $k_{\text{goe}}$  is the rate constant [ $\text{mol}/\text{s}$ ],  $IAP_{\text{goe}}$  and  $K_{\text{eq, goe}}$  [-] are the ion activity product and equilibrium constant of the reaction, respectively,  $E_{a,\text{goe}}$  is the activation energy of the reaction [ $\text{cal}/\text{mol}$ ]. The rate constants and thermodynamic parameters controlling the abiotic dissolution and precipitation of the minerals were taken from the literature and are summarized in Table 3.

### 3.2. Flow, transport and physical processes

The simulations were performed by considering partially saturated conditions with advective–dispersive transport in the aqueous phase and diffusive transport in the gas phase. The flow of water in the unsaturated porous medium was described using the generalized Richard's equation (Li et al., 2021):

$$n_w S_s \frac{\partial h}{\partial t} + \theta_t \frac{\partial n_w}{\partial t} - \frac{\partial}{\partial z} \left[ K^*(h) \left( \frac{\partial h}{\partial z} - 1 \right) \right] - q_s = 0 \quad (9)$$

where  $n_w$  is the water saturation [-],  $S_s$  is the specific storage coefficient [ $\text{m}^{-1}$ ],  $h$  is the hydraulic head [ $\text{m}$ ],  $z$  is the vertical coordinate [ $\text{m}$ ],  $K^*$  is the hydraulic conductivity, and  $q_s$  is a source/sink term. The water retention properties (i.e.,  $S_s$  and  $k_{rw}$ ) were described with the van Genuchten-Mualem model (Mualem, 1976; van Genuchten, 1980; see the Supplementary Material for more details).

The governing mass conservation equation describing the reactive transport of aqueous and gas species can be written as:

$$\frac{\partial}{\partial t} (\theta_w C_{w,i}) + \frac{\partial}{\partial t} (\theta_g C_{g,i}) = \frac{\partial}{\partial z} \left( \theta_w D_{L,i}^w \frac{\partial}{\partial z} C_{w,i} \right) + \frac{\partial}{\partial z} \left( \theta_g D_{P,i}^g \frac{\partial}{\partial z} C_{g,i} \right) - \frac{\partial}{\partial z} \theta_w v C_{w,i} - \sum_{k=1}^{N_k} v_{ik} R_k - \sum_{m=1}^{N_m} v_{im} R_m \quad (10)$$

where the indices  $w$  and  $g$  refer to the aqueous and gas phases, respectively,  $C_i$  [ $\text{mol}/\text{L}$ ] is the concentration of the primary species  $i$ ,  $D_{L,i}^w$  and  $D_{P,i}^g$  [ $\text{m}^2/\text{s}$ ] are the effective dispersion and diffusion coefficients in the aqueous and gas phases, respectively,  $\theta_w$  and  $\theta_g$  [-] are the water-filled and gas-filled porosities, respectively with the total porosity  $\theta_t = \theta_w + \theta_g$ ,  $v$  is the seepage velocity [ $\text{m}/\text{s}$ ],  $v_{ir}$  [-] is the stoichiometric coefficient for species  $i$  in the aqueous reaction  $r$  proceeding at a rate  $R_r$  [ $\text{mol}/\text{L}/\text{s}$ ],  $v_{im}$  [-] is the stoichiometric coefficient for species  $i$  in the mineral transformation reaction  $m$  proceeding at a rate  $R_m$  [ $\text{mol}/\text{L}/\text{s}$ ].

The hydrodynamic dispersion coefficients of aqueous species were calculated with the linear parameterization:

$$D_{L,i}^w = D_{P,i}^w + \alpha v \quad (11)$$

where  $D_{P,i}^w$  is the effective diffusion coefficient and  $\alpha$  is the dispersivity (0.1  $\text{m}$ ; Jardine et al., 1999; Zhou et al., 2007; Bao et al., 2017). Both effective pore diffusion coefficients for water and gas phase were calculated based on the semi-empirical formulation of Millington and Quirk (1961) to account for the local tortuosity:

$$D_{P,i}^w = D_0^w \theta_t^{1/3} n_w^{7/3} \quad (12)$$

$$D_{P,i}^g = D_0^g \theta_t^{1/3} n_g^{7/3} \quad (13)$$

where  $D_0^w$  and  $D_0^g$  are the molecular diffusion coefficients equal to  $1 \times 10^{-9} \text{ m}^2/\text{s}$  and  $5 \times 10^{-6} \text{ m}^2/\text{s}$  for the aqueous and gas species, respectively;  $n_w$  and  $n_g$  are the water and gas phase saturations, respectively with  $n_w + n_g = 1$ . The equilibrium mass-transfer of a species  $i$  between aqueous and gas phase was simulated using Henry's law:

$$H_i = \frac{C_{g,i}}{C_{w,i}} \quad (14)$$

where  $H_i$  is the Henry's law coefficient of species  $i$  (see Table S2).

The evolution of the porous matrix induced by the transformation of the mineral assemblage and its impact on the transport of aqueous species and the biogeochemical reactions were explicitly considered in the model by simulating the change in porosity, permeability, and exposed surface area (Carrier, 2003; Navarre-Sitchler et al., 2011; Seigneur et al., 2019; see Section S2 of the Supplementary Material for more details). The initial volume fractions of the minerals ( $\theta_{m,0}$ , Table 1) were calculated from the mass fractions measured with XRD using the molar mass and molar volumes of the respective minerals. Throughout this work, physical processes refer to meteoric water infiltration, gas diffusion, and pore size evolution related to the transformation of the mineral assemblage.

### 3.3. Numerical implementation

The model was implemented in the finite volume reactive transport code CrunchTope (Steeffel and Lasaga, 1994; Steefel et al., 2015). The capability to calculate partially saturated flow via the Richards equation has been recently added to CrunchTope as part of this work. The governing partial differential equations are solved with a global implicit reactive transport approach (GIMRT; Steefel and Lasaga, 1994; Steefel and Yabusaki, 1996; Steefel and MacQuarrie, 1996), which makes it possible to simultaneously simulate the transport and reaction processes with an implicit backwards Euler method and an upwind differencing scheme for advective transport. Newton's method is to solve the system of differential equations. GIMRT is particularly important in this study as it allows us to perform simulations over millennial time scale (in this case: 15,000 years) at affordable computational

**Table 3**  
Kinetic model parameters controlling the abiotic dissolution/precipitation of minerals.

Dissolution/precipitation of silicate, carbonate and clay minerals						
	Albite	Calcite	Chlorite	Dolomite	Illite	Quartz
Equilibrium constant at 25°C log $K_{eq,m}$ [-]	3.00 <sup>(a)</sup>	1.85 <sup>(b)</sup>	68.38 <sup>(c)*</sup>	3.53 <sup>(a)</sup>	6.58 <sup>(d)</sup>	-3.73 <sup>(e)</sup>
H <sub>2</sub> O dependency, effective rate constant $k_{m,H_2O}$ [mol/m <sup>2</sup> /s]	2.75 × 10 <sup>-13</sup> <sup>(f)</sup>	1.55 × 10 <sup>-6</sup> <sup>(f)</sup>	7.76 × 10 <sup>-12</sup> <sup>(f)</sup>	2.51 × 10 <sup>-9</sup> <sup>(f)</sup>	1 × 10 <sup>-15</sup> <sup>(g)</sup>	1.02 × 10 <sup>-14</sup> <sup>(f)</sup>
H <sub>2</sub> O dependency, activation energy $E_{a,m,H_2O}$ [kcal/mol]	16.68 <sup>(f)</sup>	5.62 <sup>(f)</sup>	21.03 <sup>(f)</sup>	22.78 <sup>(f)</sup>	3.35 <sup>(g)</sup>	20.96 <sup>(f)</sup>
H <sup>+</sup> dependency, effective rate constant $k_{m,H^+}$ [mol/m <sup>2</sup> /s]	10 <sup>-10.16</sup> <sup>(f)</sup>	10 <sup>-0.3</sup> <sup>(f)</sup>	10 <sup>-12.52</sup> <sup>(f)</sup>	10 <sup>-3.76</sup> <sup>(f)</sup>	10 <sup>-11.7</sup> <sup>(g)</sup>	-
H <sup>+</sup> dependency, exponent $x_{1,m}$ [-]	0.457 <sup>(f)</sup>	1.00 <sup>(f)</sup>	0.49 <sup>(f)</sup>	0.50 <sup>(f)</sup>	0.60 <sup>(g)</sup>	-
H <sup>+</sup> dependency, activation energy $E_{a,m,H^+}$ [kcal/mol]	15.54 <sup>(f)</sup>	3.44 <sup>(f)</sup>	21.03 <sup>(f)</sup>	13.55 <sup>(f)</sup>	10.99 <sup>(g)</sup>	-
OH <sup>-</sup> dependency, effective rate constant $k_{m,OH^-}$ [mol/m <sup>2</sup> /s]	10 <sup>-7.59</sup> <sup>(f)</sup>	-	-	-	10 <sup>-12.3</sup> <sup>(g)</sup>	-
OH <sup>-</sup> dependency, exponent $x_{2,m}$ [-]	0.572 <sup>(f)</sup>	-	-	-	0.6 <sup>(g)</sup>	-
OH <sup>-</sup> dependency, activation energy $E_{a,m,OH^-}$ [kcal/mol]	16.97 <sup>(f)</sup>	-	-	-	16.01 <sup>(g)</sup>	-
CO <sub>2</sub> dependency, effective rate constant $k_{m,CO_2}$ [mol/m <sup>2</sup> /s]	-	10 <sup>-4.99</sup> <sup>(f)</sup>	-	-5.37 <sup>(f)</sup>	-	-
CO <sub>2</sub> dependency, exponent $x_{3,m}$ [-]	-	1.00 <sup>(f)</sup>	-	0.5 <sup>(f)</sup>	-	-
CO <sub>2</sub> dependency, activation energy $E_{a,m,CO_2}$ [kcal/mol]	-	8.46 <sup>(f)</sup>	-	10.92 <sup>(f)</sup>	-	-
Oxidative dissolution of pyrite and precipitation/dissolution of goethite						
Effective rate constant $k_{pyr,O_2}$ [mol/m <sup>2</sup> /s]	7.94 × 10 <sup>-9</sup> <sup>(h)</sup>					
Exponent $x_{pyr,1}$ [-]	0.5 <sup>(h)</sup>					
Exponent $x_{pyr,2}$ [-]	-0.11 <sup>(h)</sup>					
Effective rate constant $k_{pyr,Fe^{3+}}$ [mol/m <sup>2</sup> /s]	3.16 × 10 <sup>-10</sup> <sup>(h)</sup>					
Exponent $x_{pyr,3}$ [-]	0.3 <sup>(h)</sup>					
Exponent $x_{pyr,4}$ [-]	-0.47 <sup>(h)</sup>					
Exponent $x_{pyr,5}$ [-]	-0.32 <sup>(h)</sup>					
Goethite equilibrium constant at 25°C log $K_{eq,goe}$ [-]	0.36 <sup>(i)</sup>					
Goethite, effective rate constant $k_{goe}$ [mol/s]	1.15 × 10 <sup>-8</sup> <sup>(f)</sup>					
Goethite, activation energy $E_{a,goe}$ [kcal/mol]	20.67 <sup>(f)</sup>					

<sup>(a)</sup> Robie and Hemingway (1995).

<sup>(b)</sup> Blanc et al. (2012).

<sup>(c)</sup> Helgeson et al. (1978).

<sup>(d)</sup> Köhler et al. (2003).

<sup>(e)</sup> Richet et al. (1982).

<sup>(f)</sup> Palandri and Kharaka (2004).

<sup>(g)</sup> Godderis et al. (2006).

<sup>(h)</sup> Williamson and Rimstidt (1994).

<sup>(i)</sup> Majzlan et al. (2003).

\* For chlorite, the thermodynamic properties of clinocllore 14 Å were considered based on the similar properties of these minerals.

cost. The thermodynamic database Thermoddem (Blanc et al., 2012) was used to calculate the aqueous speciation and reaction between dissolved species. CrunchTope partitions the aqueous species between primary and secondary species. Primary species are used for mass conservation transport equation while secondary species are explicitly considered for aqueous reactions and mineral transformation calculations. The model considers 17 primary and 39 secondary species in the aqueous phase and 3 species in the gas phase: O<sub>2(g)</sub>, CO<sub>2(g)</sub>, and N<sub>2(g)</sub> (see Table S2 for a complete list of species).

The simulations were performed using a vertical 8 m long 1-D domain discretized into 80 grid cells ( $\Delta x = 10$  cm). Unaltered shale bedrock was assumed to uniformly compose the porous matrix at the start of the simulation using the mineral composition of the parent rock determined with the quantitative XRD analyses and presented in Table 1. Infiltration of meteoric water was simulated by defining a flux boundary condition at the top of the model domain with an average water infiltration rate of 300 mm/year. The hydrochemical composition of the infiltrating water was assumed constant throughout the simulation using data from the National Atmospheric Deposition Program (Table S3). The DOC concentration of the infiltrating water was calibrated to simulate the replenishment of fresh litter/plant-derived organic matter and to reproduce the DOC and TOC levels measured in groundwater and the upper soil layer, respectively. Furthermore, gas exchange between the subsurface and the atmosphere was controlled by defining a Dirichlet boundary condition with fixed partial pressure of reactive gases in the atmosphere at the altitude of the hillslope (i.e.,  $p_{O_2} = 1.68 \times 10^{-1}$  bar,  $p_{N_2} = 6.24 \times 10^{-1}$  bar, and  $p_{CO_2} = 3.17 \times 10^{-4}$  bar).

To decrease the computational cost of the simulations, the distribution of water saturation determined using the Richards' equation (Eq. (8)) was assumed constant in time by using the lower water saturation conditions that prevail through most of the year (Fig. S2). The model also accounted for the effect of temperature on the biogeochemical reactions (e.g., Arora et al., 2016) by defining a vertical temperature gradient based on the temperature measurements performed at multiple depths in the monitoring wells (Fig. S2).

Calibration was performed to develop a single set of parameters capable of reproducing the vertical profiles of the mineral concentrations, solid carbon content (TOC), aqueous concentrations of organic carbon (DOC), and CO<sub>2</sub> concentration in the gas phase measured in all three monitoring wells. The calibration was restrained to model parameters controlling the mass-transfer of organic matter between the aqueous and solid phases ( $k_{DOM}$  and  $K_{DOM}$ ), the aerobic respiration of organic matter ( $\mu_{max,S}$ ,  $K_{m,S}$ , and  $K_{m,TEA}$ ), and the fresh litter/plant-derived DOC concentration in the infiltrating water. More details on parameters calibration are provided in Section S5 of the Supplementary Material.

## 4. Results

### 4.1. Long-term evolution of the weathering front

Fig. 3 compares the simulated and measured mineral concentrations and displays the simulated change in porosity in the three monitoring wells. The results illustrate the presence of a weathering front within the upper two to four meters of the hillslope.

The weathering front is primarily characterized by the depletion of dolomite (Fig. 3a-c) and pyrite (Fig. 3d-f) and the precipitation of secondary mineral phases: calcite (Fig. 3i) and goethite (Fig. 3j-l). The depth of the weathering front (i.e., defined as the zone where dolomite and pyrite concentrations are lower than in the parent rock) coincides with the greatest depth of the water table, but differs among the three wells. In particular, the weathering front and water table are significantly shallower in PLM3 (water table is 2.5 m) located at the toe-slope and closer to the floodplain. In comparison, wells PLM1 and PLM2 are located upslope and their water tables are 4 and 4.1 m, respectively.

Measured data in wells PLM1 and PLM3 show that the low amounts of calcite initially present in the bedrock (i.e., 1.2 wt%)

is depleted within the top soil, but that localized secondary calcite precipitation occurs below the weathering front leading to a peak in calcite concentration (Fig. 3i). The detected amount of calcite is higher in PLM3 (maximum concentration is 6.9 wt%) compared to PLM1 (maximum concentration is 2.5 wt%) as shown by the broad concentration peak measured between 2.13 and 3.96 m bgs in PLM3 (Fig. 3i). Low amounts of goethite are also observed within the top two meters in well PLM3 with concentrations mirroring that of pyrite (Fig. 3l), which indicates that the iron released upon the dissolution of pyrite precipitates predominantly into iron oxides. Results for the clay and silicate minerals are presented in Fig. S3 and show that their alteration remains minor as these minerals are relatively insoluble over the time scale considered.

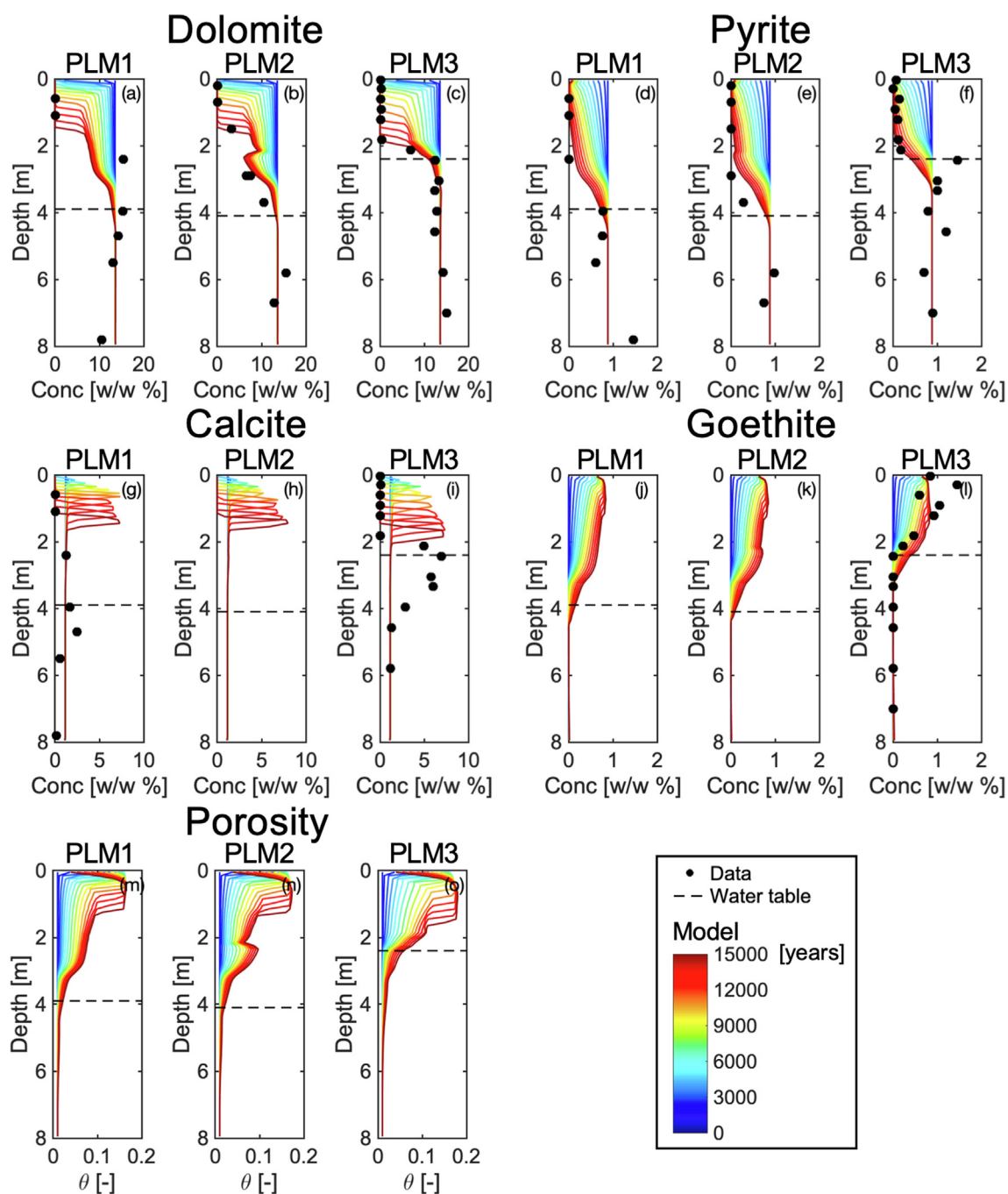


Fig. 3. Measured mineral concentration profiles in the three monitoring wells and simulated evolution of the mineral composition and porosity. Simulated concentration profiles are plotted at 1000 years intervals. Goethite concentrations in PLM1 and PLM2 and calcite concentrations in PLM2 were not reported by Wan et al. (2021).

The model successfully reproduces the measured primary mineral concentration profiles and captures the weathering front in the three wells (i.e., comparison between data and model results at 15,000 years are shown as red lines; Table S5 presents a model accuracy matrix for the different measured aqueous, gas, and solid concentrations). The simulated long-term evolution of the mineral profiles displayed in Fig. 3 shows the progressive depletion of dolomite and pyrite and the precipitation of goethite and calcite and emphasizes the complex spatiotemporal behavior of weathering. In particular, pyrite is removed faster and shows a sharper depletion front than that of dolomite. This difference is particularly clear in wells PLM1 and PLM2, which have thicker unsaturated zones (Fig. 3a–b and Fig. 3d–e) compared to PLM3 where near-complete removal of dolomite and pyrite occurs during the time period considered (Fig. 3c and Fig. 3f). Furthermore, the dissolution rates of the parent minerals vary significantly as the weathering proceeds. For instance, the dissolution of dolomite increases during the last 5,000 years within the upper two meters as illustrated by the greater distance between the mineral concentration profiles (Fig. 3a–c). In contrast, the dissolution of pyrite is initially fast (greater distance between the lines of the concentration profile) and decreases with time (Fig. 3d–f). The dissolution of both dolomite and pyrite are strongly limited close to the water table as shown by the shorter distances between the concentration profiles at depth greater than 2 m bgs.

Furthermore, the outcomes of the simulations show that calcite precipitates underneath the dolomite reaction front (i.e., location where dolomite dissolution rate is highest) and re-dissolves once dolomite is depleted, thus leading to a progressive shift in the calcite concentration peak (Fig. 3g–i). Calcite has a lower solubility under groundwater temperature conditions, and therefore precipitates at the expense of dolomite (Szramek et al., 2007). Although the model can reproduce the maximum calcite concentration measured in the wells, the simulated calcite concentration peak is narrower than the one measured in PLM3. This discrepancy might reflect the importance of the lateral flow below the water table that leads to concentration build-up and/or transverse dispersion of calcium and carbonate and ultimately results in more widespread precipitation of calcite (i.e.,  $\text{Ca}^{2+}$  plume released from the dolomite dissolution broadens downgradient; e.g., Haberer et al., 2015).

Fig. 3m–o present the simulated porosity profiles and show that the depletion of the primary minerals in the weathering front induces an increase in porosity with a maximum  $\theta_t = 0.17$  in the three wells. The complex pattern in simulated porosity primarily results from its dependency to dolomite dissolution (Fig. 3a–c) as dolomite occupies a significant volume fraction in the parent rock (12.6 vol%). In contrast, the dissolution of pyrite and calcite (1.2 vol% and 0.5 vol%, respectively) as well as minor dissolution of albite and chlorite (<2 vol%) have a limited impact on the porosity. The simulated porosity value in the upper part of the profiles is in agreement with the experimentally-determined porosity of the weathered shale ( $\theta_{\text{tot}} = 0.2$ ), but underestimates the soil porosity ( $\theta_{\text{tot}} = 0.4$ ; first meter below bgs). This discrepancy can be attributed to other physical and biological mechanisms (e.g., root growths and decay, bioturbation, freeze–thaw cycles) that are not included in the model but may contribute to a significant increase in porosity in top soils (Sorensen et al., 2020; Meurer et al., 2020).

#### 4.2. Spatial distribution of organic carbon

Fig. 4 presents the comparison between simulation outcomes and the depth-discretized measurements of organic carbon and  $\text{CO}_2$  concentrations at the three spatial locations. The results show complex spatial distribution of organic carbon and strong  $\text{CO}_2$

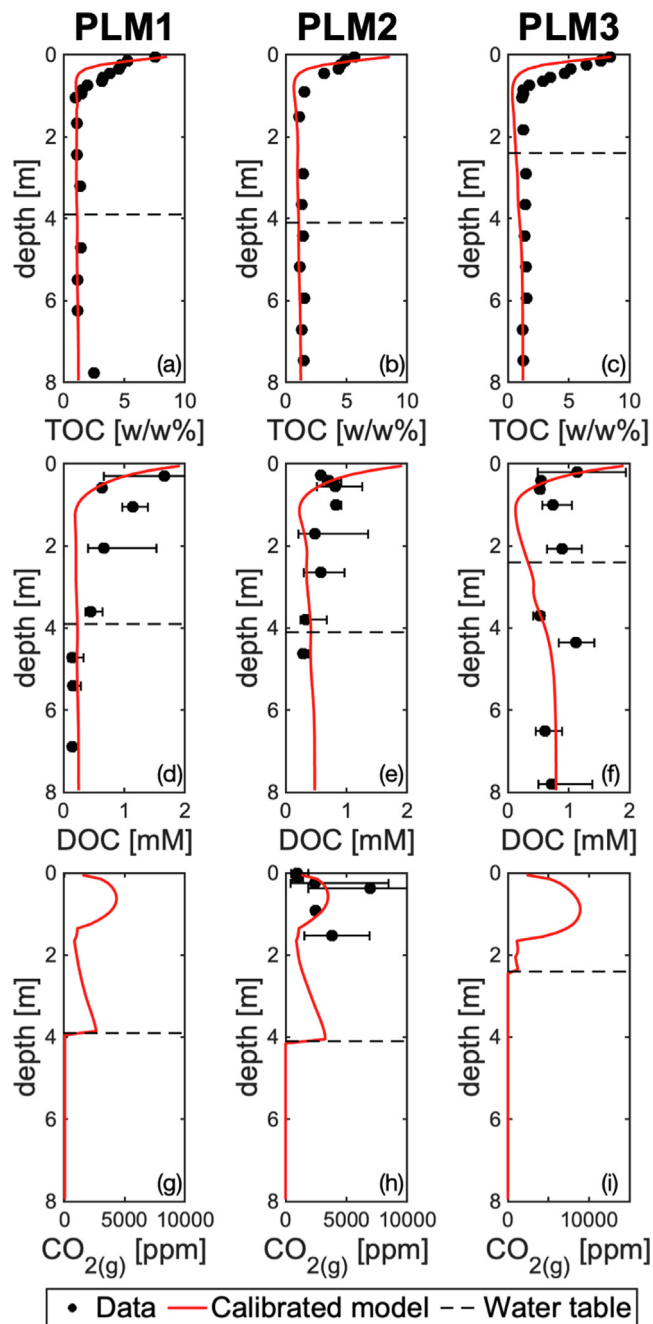


Fig. 4. Present-day measured and simulated organic carbon concentrations profiles in the solid phase (a–c) and aqueous phase (d–f) and carbon dioxide concentrations in the gas phase (g–i). The dots show the average concentrations measured at a specific depth and the error bars show the amplitude of seasonal variations in concentrations. Lines show simulation outcomes at  $t = 15,000$  years.  $\text{CO}_{2(\text{g})}$  concentrations were only measured in the vicinity of PLM2.

emissions indicating that microbial respiration is a significant process along the hillslope transect.

Fig. 4a–c show that the TOC concentration is vertically heterogeneous but relatively homogeneous in the longitudinal direction of the hillslope ([1.0 – 8.4] wt%). Low TOC concentration reflects the composition of shale below 1 m (~1 wt%) and increases sharply within the top 1 m, which represents a depth shallower than the weathering front (i.e., 4 m, 4.1 m, and 2.5 m in wells PLM1, PLM2, and PLM3, respectively). In contrast, the measured DOC con-

centrations are in the range [0.12 – 1.66] mM and only show a slight increase in the upper part of the subsurface, which is more pronounced in PLM1 (Fig. 4d-f).

The  $\text{CO}_{2(g)}$  concentrations measured in the vadose zone are significantly higher (i.e., average concentrations are in the range [940 – 6960] ppm; Fig. 4g-i) than the atmospheric  $\text{CO}_{2(g)}$  concentration (~400 ppm), indicating significant  $\text{CO}_{2(g)}$  emissions to the atmosphere resulting from aerobic respiration in the subsurface. In comparison, measured  $\text{CH}_{4(g)}$  concentrations are low with values lying close to the detection limit of the instrument (i.e., < 2.1 ppm; not shown here) showing that methanogenesis does not significantly contribute to the cycling of carbon at our study site.

The model can satisfactorily reproduce the complex profiles of carbon concentrations measured in the three wells ( $R^2 = 0.82$  and  $0.48$  for TOC and DOC, respectively, Table S5). In particular, the model captures the accumulation of fresh litter/plant-derived organic carbon in the top soil (Fig. 4a-c) and the concentration of DOC released from the shale at depth (Fig. 4d-e) using the calibrated parameters controlling the mass-transfer of organic matter between the aqueous and the solid phases ( $k_{DOM}$  and  $K_{eq,DOM}$  shown in Table 5). The simulated distribution of shale-associated and fresh litter/plant-derived organic carbon is shown in Fig. S4. Furthermore, the rate constant controlling the release of DOM from shale ( $k_{DOM} = 1.28 \times 10^{-8}$  mol/m<sup>2</sup>/s) is in agreement with the rate of DOC release estimated experimentally by Schillawski and Petsch (2008) (i.e.,  $R_{DOM} = \sim 3 \times 10^{-7}$  mol/s considering the amount of shale OM observed at our site and shown in Table 1). Finally, the model can reproduce the  $\text{CO}_{2(g)}$  levels measured in the vadose zone, which validates the simulated rates of aerobic respiration since  $\text{CO}_{2(g)}$  is the end product of the microbially-mediated reaction. The kinetic parameters controlling the aerobic respiration of fresh litter/plant-derived and shale-derived organic matter are provided in Table 4 and show that the simulated aerobic respiration rate of fresh litter/plant-derived OM is higher than shale-derived organic matter.

#### 4.3. Processes controlling the weathering of shale

The calibrated model is used to quantitatively evaluate the roles of the physical, microbial, and geochemical processes controlling the weathering of shale. To do so, we define five modeling scenarios (denoted A-E) in which mechanisms are individually removed from the calibrated model (Table 5). Here, we use PLM3 as our base case and focus on the effects of physical mechanisms (i.e., gas diffusion and porosity development related to the dissolution of primary minerals) and aerobic respiration. Further, both the total and individual impacts of fresh litter/plant-derived and shale-associated organic matter degradation are evaluated.

Fig. 5 displays the outcomes of the simulations and the comparison with the measured mineral concentrations in well PLM3 (similar results are presented for the two other monitoring wells in

Fig. S5). The simulation performed in scenario A (red line in Fig. 5a-e) shows that the dissolution of primary minerals (dolomite and pyrite) and the precipitation of secondary minerals (calcite and goethite) are limited significantly when gas diffusion is not included in the model. This result indicates that the continuous ingress of atmospheric gases is the primary physical mechanism driving the weathering of shale. In particular, the delivery of reactants via diffusion in the gas phase, such as  $\text{O}_2$  that is directly involved in the dissolution of pyrite and the precipitation of goethite (see reaction stoichiometries in Table 2), is relatively rapid (i.e., diffusion coefficient almost four orders of magnitude higher in the gas phase than in the aqueous phase). The slight decrease in mineral concentration simulated in the upper part of the profile in the absence of gas diffusion takes place as the infiltrated water contains low concentrations of dissolved  $\text{O}_2$  and  $\text{CO}_2$  in equilibrium with the atmosphere. Furthermore, simulation outcomes of scenario B (dotted purple line in Fig. 5a-e) show that the increase in porosity resulting from the loss of parent minerals plays a significant role in the transformation of the mineral assemblage. In fact, when a constant porosity is assumed, mineral reactions decrease with significantly lower dolomite dissolution (Fig. 5a), and to a lesser extent, lower pyrite dissolution (Fig. 5b) and goethite precipitation (Fig. 5d). This result indicates that the increase in porosity is an important mechanism for the weathering of shale by allowing both an increase in reactive gas ingress into the subsurface and a higher contact between the reactants and the mineral surfaces (see details on the evolution of the porous matrix in the Supplementary Material).

Modeling outcomes in scenario C (blue lines in Fig. 5f-j) demonstrate that aerobic respiration is a critical mechanism for the development of the weathering front. In fact, when this microbially-mediated reaction is not included, the dissolution of carbonate minerals is significantly reduced (dolomite and calcite in Fig. 5f and 4 h, respectively), whereas the dissolution of pyrite is enhanced (Fig. 5g). The impact of aerobic respiration on dolomite dissolution can be explained as this microbially-mediated reaction leads to significant production of  $\text{CO}_2$  that acidifies the pore water and triggers the dissolution of dolomite. In contrast, the consumption of  $\text{O}_2$  during aerobic respiration limits the dissolution of pyrite at depth (Fig. 5g). The slight dissolution of dolomite visible in Scenario C is induced by the atmospheric  $\text{CO}_2$  ingress and the production of sulfuric acid during pyrite dissolution (Fig. S6).

Scenarios D and E (green full line and orange dashed line, respectively in Fig. 5f-j) explore the individual impacts of the aerobic respiration of fresh plant-litter-derived and shale-associated organic, respectively. Simulation outcomes show significantly lower carbonate minerals dissolution when the aerobic respiration of fresh OM is discarded (scenario D; green full line in Fig. 5f and 5 h), while no significant change in the mineral assemblage transformation is observed when the reactivity of shale-associated OM is inhibited (scenario E; orange dashed line in Fig. 5f and 5 h). This difference suggests that aerobic respiration of shale-associated

**Table 4**

Calibrated model parameters controlling the availability of organic matter and the aerobic respiration. 95% confidence intervals of the calibrated parameters are shown in brackets.

	Shale OM	Fresh OM
<b>Exchange between aqueous phase and solid matrix</b>		
$k_{DOM}$ [mol/m <sup>2</sup> /s]	$1.28 \times 10^{-8}$ [ $1.81 \times 10^{-9}$ ; $5.22 \times 10^{-8}$ ]	$1.90 \times 10^{-20}$ [ $1.17 \times 10^{-20}$ ; $6.12 \times 10^{-19}$ ]
$\log K_{eq,DOM}$ [-]	-3.32 [-3.6; -3.1]	-9.35 [-9.50; -7.62]
<b>Aerobic respiration</b>		
$\mu_{max,S}$ [mol/L/s]	$6.02 \times 10^{-11}$ [ $2.98 \times 10^{-11}$ ; $1.01 \times 10^{-10}$ ]	$2.00 \times 10^{-10}$ [ $1.95 \times 10^{-10}$ ; $2.00 \times 10^{-10}$ ]
$K_{m,S}$ [mol/L]		$1.31 \times 10^{-4}$ [ $6.33 \times 10^{-5}$ ; $6.25 \times 10^{-4}$ ]
$K_{m,TEA}$ [mol/L]		$3.00 \times 10^{-6}$ [ $3.00 \times 10^{-6}$ ; $1.15 \times 10^{-5}$ ]

**Table 5**  
Physical and biogeochemical mechanisms considered in the modeling scenarios.

	Calibrated		Scenarios				
	model	A	B	C	D	E	
<b>Gas diffusion</b>	Yes	No	Yes	Yes	Yes	Yes	
<b>Porosity evolution</b>	Yes	Yes	No	Yes	Yes	Yes	
<b>Aerobic respiration - fresh OM</b>	Yes	Yes	Yes	No	No	Yes	
<b>Aerobic respiration - shale OM</b>	Yes	Yes	Yes	No	Yes	No	

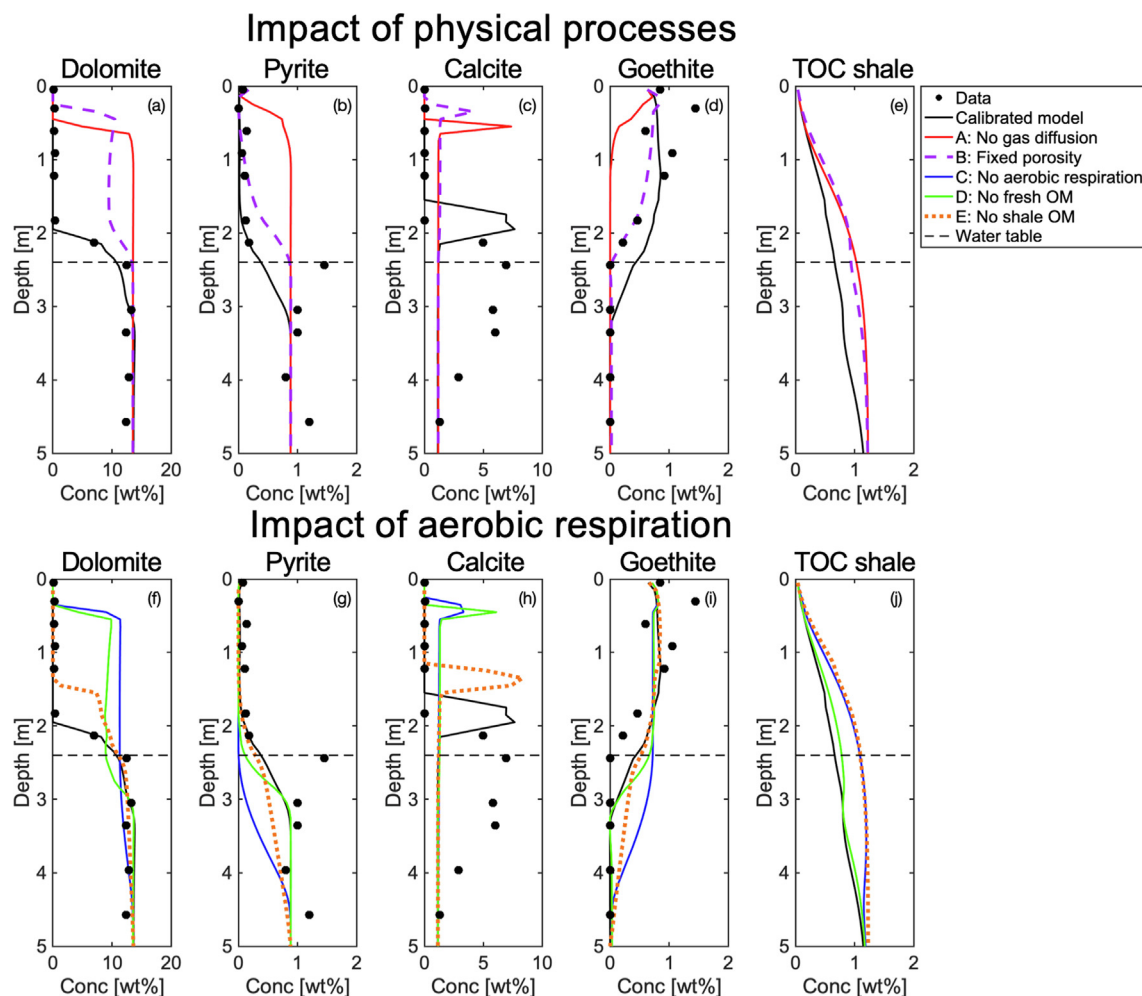


**Fig. 5.** Comparison between present-day measured and simulated mineral concentration profiles in PLM3 as impacted by physical (a–e) and biological mechanisms (f–j). The simulations are performed using five modeling scenarios denoted A–E, which are described in more details in Table 5. Lines show simulation outcomes at  $t = 15,000$  years.

organic matter plays a minor role in the mineral weathering compared to the aerobic respiration of fresh litter/plant-derived organic matter.

As shown by the simulated decrease in TOC when aerobic respiration of shale OM is discarded (Scenarios C and E in Fig. 5j), significant depletion of shale-associated TOC is simulated from the release of shale-derived DOM. In order to test if the simulated release and subsequent elution of shale-derived DOM don't result in underestimating the importance of shale OM aerobic respiration, we perform additional simulations in which direct oxidation of solid shale OM is considered (Petsch et al., 2000; Bolton et al., 2006). Outcomes of the simulations are shown in Fig. S7 and S18 and confirm that the aerobic respiration of shale OM has a limited

influence on the weathering of shale at our site. The results also corroborate our conceptual model which includes the release of labile DOM from shale that subsequently undergoes aerobic respiration.

## 5. Discussion

The model-based interpretation through the formulation of modeling scenarios has allowed us to identify the key processes leading to the alteration of shale bedrock and the development of the observed weathering front. In particular, we found that the ingress of atmospheric oxygen via the gas phase directly induces the oxidative dissolution of pyrite, although it is limited by the

degradation of fresh organic matter through microbial respiration. This microbially-mediated reaction generates carbon dioxide that acidifies the pore water and triggers the dissolution of carbonate minerals. Thus, aerobic respiration exerts a fundamental control on the depletion fronts of carbonate and sulfide minerals through the balance between oxygen consumption and carbon dioxide production. In the following, we further analyze and discuss the spatial and temporal evolution of the weathering front and the implications of the presence of different types of organic matter having different spatial distribution and reactivities for the weathering of shale. We focus on one location of the hillslope transect (PLM3) and similar results for the two other monitoring wells (PLM1 and PLM2) are provided in the [Supplementary Material](#).

### 5.1. Rates and mechanisms controlling pyrite and dolomite depletion fronts

In order to analyze the dynamics of the long-term alteration of shale, we computed the advance of the depletion fronts, expressed as 5 %, 50 %, and 95 % of the initial amount present the shale bedrock, of the pyrite and dolomite. [Fig. 6](#) illustrates the results obtained in well PLM3 and shows important differences regarding the depletion of the two minerals.

As shown by the dissociated depletion fronts expressed at 5 %, 50 %, and 95 % of the amount of mineral initially present ([Fig. 6a–b](#)), the dissolution of pyrite and dolomite occur throughout the unsaturated zone over the time period considered. While pyrite dissolution rate is relatively uniform within the unsaturated zone as shown by the similar advance rates of the 50 % and 95 % depletion fronts, the advance of the dolomite depletion front shows a more complex behavior. In particular, a small fraction of dolomite is rapidly consumed throughout the unsaturated zone (green dotted line in [Fig. 6b](#)), whereas the propagation of fronts characterized by higher depletion of dolomite (greater than 50 %) is significantly slower. Furthermore, the 50 % and 95 % depletion fronts overlap, indicating that the reaction front of dolomite is localized and shifts downward as dolomite becomes depleted (black line and orange dashed line in [Fig. 6b](#)). Such heterogeneous depletion of dolomite within the unsaturated zone (i.e., dissolution of a small fraction of dolomite throughout the unsaturated zone followed by a local-

ized reaction front) leads to the development of a complex non-planar weathering front as shown in [Fig. 3a–b](#).

Furthermore, the model indicates that the depletion rate of dolomite ( $[7 \times 10^{-2} - 1.5 \times 10^{-1}] \text{ mol/m}^3/\text{year}$ ) is significantly higher than that of pyrite ( $< 2.5 \times 10^{-2} \text{ mol/m}^3/\text{year}$ ; [Fig. 6c](#)). However, the removal of dolomite relative to its initial mass is slower ([Fig. 6d](#)) due to the higher amount of dolomite in the bedrock. These results clearly highlight the dissociation between the evolution of the dolomite and the pyrite dissolution fronts and show that pyrite and dolomite dissolution are not stoichiometrically linked through the production of sulfuric acid during pyrite dissolution. In particular, the amount of pyrite is significantly lower (0.9 wt%) than that of dolomite (13.7 wt%). Therefore, the oxidative dissolution of pyrite cannot by itself induce significant carbonate mineral dissolution under the geochemical conditions considered in this study.

To further analyze the differences in the evolution of the pyrite and dolomite depletion fronts and the coupling between weathering, transport, and biogeochemical mechanisms, [Fig. 7](#) displays the spatial and temporal changes in reactant concentrations, porosity, mineral dissolution and aerobic respiration rates simulated in PLM3.

[Fig. 7a](#) and [7b](#) show that atmospheric oxygen can diffuse rapidly via the gas phase, thus triggering the dissolution of pyrite throughout the unsaturated zone. Oxygen concentration is lower at greater depth as it is consumed by both aerobic respiration and pyrite oxidation, but increases progressively in time as the primary minerals dissolve and porosity increases ([Fig. 7c](#)). At present day ( $t = 15,000$  years), the model shows that the gas and aqueous concentrations of oxygen are nearly at equilibrium with the atmosphere within the unsaturated zone and sharply decrease with depth around the groundwater table due to the higher liquid saturation ([Fig. S9](#)). The lower flux of oxygen under saturated conditions and its consumption via aerobic respiration strongly limits the dissolution of pyrite below the water table ([Fig. 7b](#); water table in PLM3 is 2.5 m bgs). Furthermore, [Fig. 7d](#) shows that aerobic respiration occurs primarily in the top soil, increases in time and generates carbon dioxide that triggers the dissolution of dolomite ([Fig. 7e](#)) through the acidification of the pore water ([Fig. 7f](#); see reaction stoichiometries in [Table 2](#)). At present day, the rate of aerobic respiration within the upper 1 m ( $\sim 0.4 \text{ mol/m}^3/\text{year}$ ) is signif-

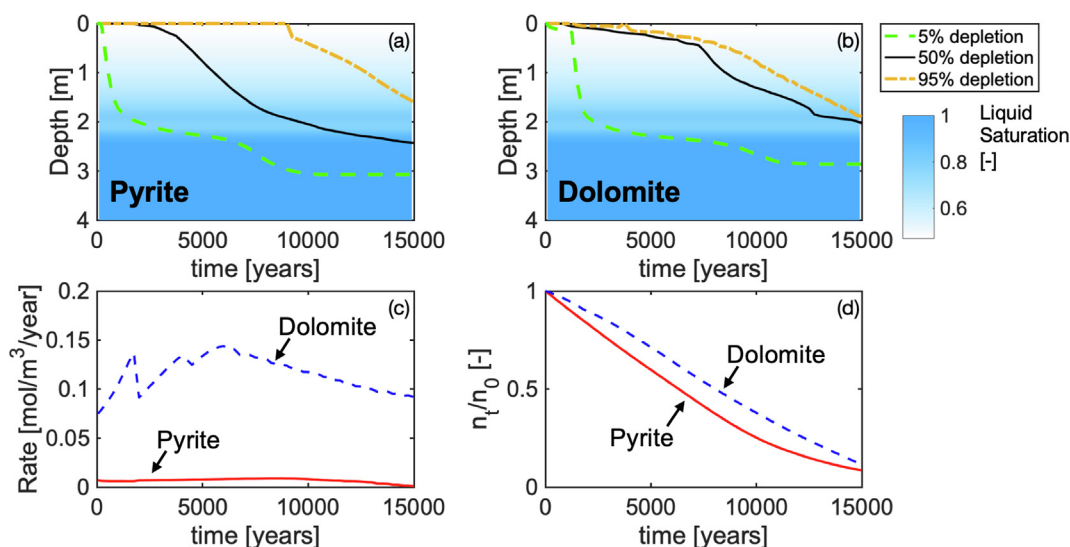


**Fig. 6.** Simulated evolution of the weathering front in well PLM3: advance of depletion fronts of pyrite (a) and dolomite (b) expressed as percentage of depleted minerals; average rate of mineral dissolution within the unsaturated zone ( $< 2.5$  m bgs) (c); fraction of depleted mineral within the unsaturated zone (d).

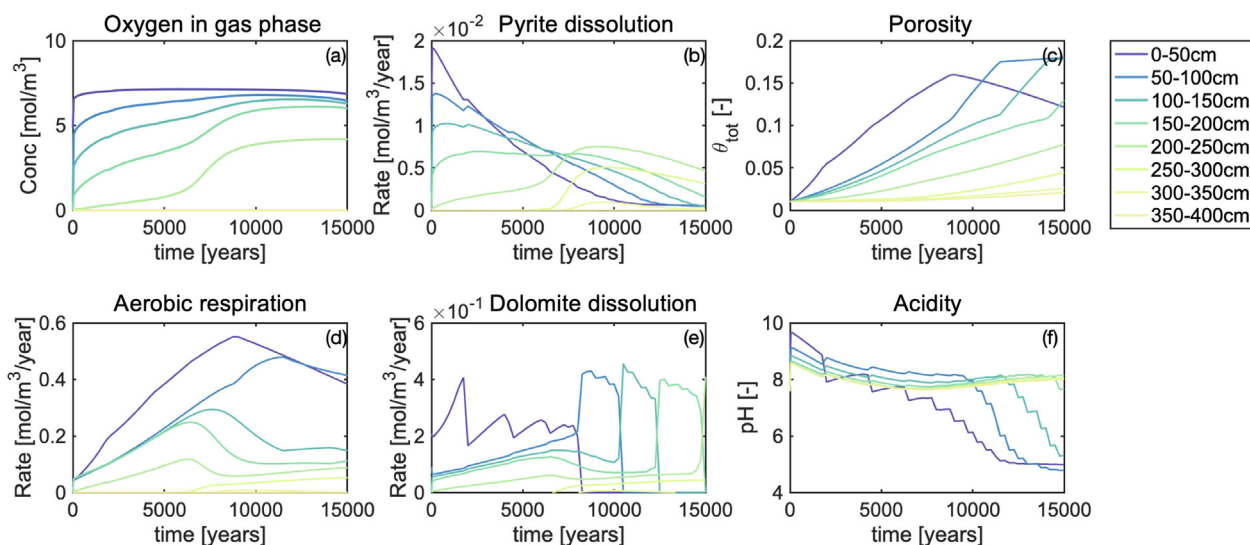


Fig. 7. Simulated evolution of the reactant concentrations, aerobic respiration rates, primary mineral dissolution rates, and porosity within selected depth intervals in PLM3.

icantly higher than that of pyrite dissolution ( $<5 \times 10^{-3}$  mol/m<sup>3</sup>/year) and is nearly equal to the maximum rate of dolomite dissolution ( $\sim 0.41$  mol/m<sup>3</sup>/year) showing that aerobic respiration is the primary driver of carbonate mineral depletion. The model shows that the protons are transported downward through groundwater infiltration leading to a localized reaction front where dolomite dissolves (Fig. 7e) to buffer the acidic pH (Fig. 7f). Additional simulations extended to 50,000 years show that the depletion front of carbonate minerals will continue to extend beneath the water table as aerobic respiration and groundwater recharge sustain the supply of protons from the top soil to the dolomite reaction front (Fig. S10).

## 5.2. Spatial distribution and reactivity of organic matter

The calibrated model was used to analyze the respective roles of the ancient and modern organic matter on shale weathering through aerobic respiration. In particular, the model allows us to quantitatively assess the vertical distribution and respective reactivities of fresh plant/litter-derived and shale-associated organic

carbon, which could not be directly inferred from the field measurements.

Fig. 8a displays the simulated relative distribution of the modern and ancient organic carbon in PLM3 after 15,000 years of chemical weathering (i.e., present). The OM distribution shows that dissolved fresh litter/plant-derived organic matter dominates in the top soil and is rapidly consumed through microbial respiration with depth (negligible concentration below 2 m). This result also highlights that the continuous infiltration of fresh organic matter has led to the accumulation of solid organic carbon close to the ground surface (Fig. 4a-c; Dwivedi et al., 2017; Chapelle, 2021) leading to the observed TOC profiles and contributing to the formation of biologically active soil. In contrast, shale-associated organic carbon represents only a minor fraction of the total carbon pool in the upper part of the profile as it has been depleted through DOM released from the solid organic matter and its exposure to atmospheric conditions. Shale OC becomes dominant with depth where bedrock remains weakly altered (shale accounts for more than 50 % of OC below 1 m).

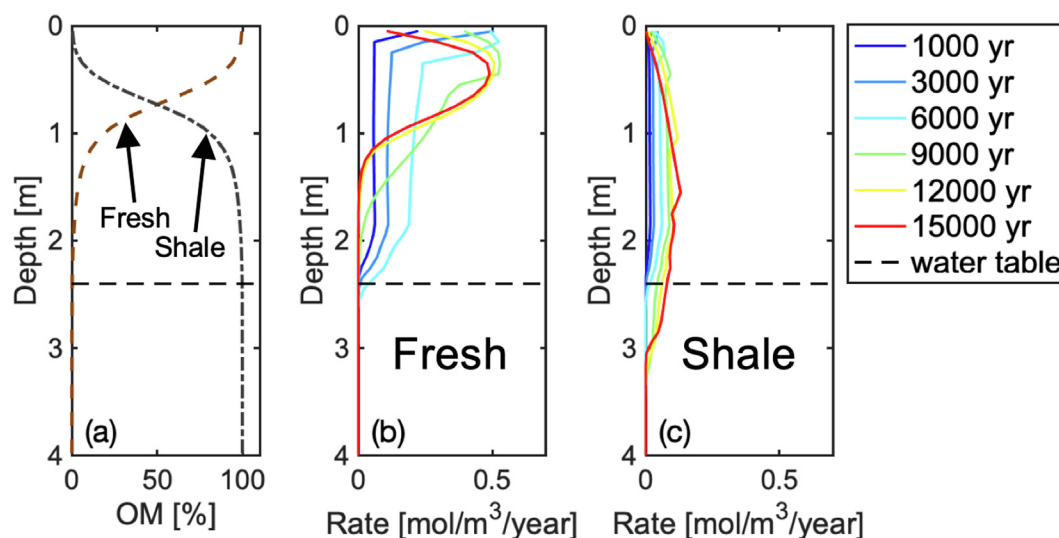


Fig. 8. Relative concentrations of fresh litter/plant-derived and shale-derived organic matter at present day ( $t = 15,000$  years) and evolution of the aerobic respiration rates simulated in PLM3.

Fig. 8b and 8c show that the simulated microbial respiration rate using fresh plant/litter-derived organic matter is higher (average and maximum rate at present in the unsaturated zone equal 0.15 and 0.49 mol/m<sup>3</sup>/year, respectively) than that of shale-derived organic matter (average and maximum rates at present in the unsaturated zone equal 0.08 and 0.13 mol/m<sup>3</sup>/year, respectively). This suggests the higher ability of microorganisms to degrade modern organic matter and corroborates the modeling scenarios presented in Section 4.2., which pointed out the predominant role of aerobic respiration of fresh litter/plant-derived organic matter on the weathering of shale. Furthermore, while the aerobic respiration of fresh organic matter is low and uniformly distributed within the unsaturated zone at early times of the simulation, it increases progressively in the first meter below the ground surface where it becomes dominant with time. This result indicates that the increase in porosity in the upper part of the subsurface due to the depletion of the primary minerals and the related increase in reactants fluxes progressively favor the aerobic respiration of organic matter within the upper 1 m. Therefore, biologically active soil represents a hotspot where most of the dissolved fresh organic matter is consumed and pore water acidification takes place before being transported downward through groundwater recharge.

The lower aerobic respiration of shale associated organic matter is more uniformly distributed due to its widespread presence in the bedrock, although the location of the rate's maximum shifts downward as shale-associated carbon gets progressively depleted (Fig. 8e).

## 6. Conclusions

In this study, we proposed and implemented a modeling approach to disentangle the complex interplay between the physical, geochemical, and biological processes controlling the long-term chemical weathering of shale with a particular focus on the role of aerobic respiration. We considered a well-instrumented hillslope transect, where detailed field investigations had revealed a stratified weathering front and heterogeneous distributions of dissolved and solid-associated organic carbon concentrations. A multiphase reactive transport model simulating the alteration of shale bedrock based on CrunchTope augmented with a newly developed Richards' equation routine was implemented to quantitatively interpret the observations. The novelty of the proposed modeling approach lies in the joint consideration of co-occurring mechanisms including: (i) the gas exchange between the subsurface and the atmosphere and the infiltration of meteoric water, (ii) the aerobic respiration driven by the continuous ingress of oxygen and the presence of organic matter, and (iii) the reactions between aqueous solutes and the complex mineral assemblage composing the solid matrix. In particular, the model explicitly accounts for the presence of ancient organic matter homogeneously distributed in the shale and the intrusion of modern organic matter from the top soil. The simulations were run for 15,000 years starting from the last glaciation period and were able to successfully reproduce the field dataset collected at various spatial locations that includes the aqueous, gas, and solid phases with a single set of model parameters.

The modelling results, verified by field observations, show that the ingress of oxygen from the atmosphere into the subsurface represents the primary driver for the weathering as it induces the conversion of pyrite into goethite and triggers aerobic respiration. The latter exerts a strong but opposite control on the depletion of sulfide and carbonate minerals as it promotes the dissolution of dolomite via the production of CO<sub>2</sub>, but limits the dissolution of pyrite at depth by consuming O<sub>2</sub>. The modeling outcomes clearly indicate that the evolution of the dolomite and pyrite depletion fronts are

stoichiometrically decoupled (i.e., low impact of sulfuric acid produced during pyrite dissolution). In fact, the development of the weathering fronts depends on the various pathways of the reactants into the subsurface as well as the rates and spatial distribution of organic matter degradation via aerobic respiration. The rapid ingress of oxygen into the subsurface via the gas phase leads to the homogeneous depletion of pyrite within the unsaturated zone. In contrast, aerobic respiration occurs predominantly in the biologically active soil due to the higher reactivity of the fresh litter/plant-derived organic matter compared to shale-associated organic carbon, where it acidifies the pore water. The subsequent transport of protons through groundwater infiltration leads to a localized reaction front for dolomite that is gradually depleted downward. The limited diffusion of reactive atmospheric gases under high water saturation conditions and the consumption of oxygen via microbially-mediated reactions limits the depletion of pyrite below the water table. In contrast, continuous input of CO<sub>2</sub> and protons via aerobic respiration and groundwater recharge can sustain the dissolution of dolomite under saturated conditions.

Our results demonstrate that the balance between carbonate and sulfide minerals consumption is determined by the availability and reactivity of fresh and shale-associated organic matter and the ability of the local microbial communities to perform aerobic respiration. Similar depletion fronts for sulfide, carbonate minerals and shale-associated organic matter have been observed elsewhere (e.g., Littke et al., 1991; Petsch et al., 2000; Wildman et al., 2004; Jin et al., 2013), which indicate that the predominant weathering processes identified in this study are valid for other shale formations. Our model represents a valuable tool that could be exported to other locations in order to further analyze the impacts of local climatic, hydrological, and geochemical conditions on the weathering of shales and black shales (Ma et al., 2011; Dere et al., 2013). The mechanistic understanding of shale weathering gained from such modeling approach will improve the interpretation of seasonal hydrochemical fluxes observed at larger scales (Winnick et al., 2017; Arora et al., 2021) and will support the refinement of global biogeochemical cycling of carbon and sulfur (Amiotte-Suchet, et al., 2003; Fox et al., 2022).

## Data availability

I have attached a Supplementary Data file and provided a link to an online open-access data repository (ESS-Dive)

## Declaration of Competing Interest

The authors declare that they have no known competing financial interests or personal relationships that could have appeared to influence the work reported in this paper.

## Acknowledgements

This work was supported by the Watershed Function Science Focus Area project at Lawrence Berkeley National Laboratory funded by the U.S. Department of Energy, Office of Science, Biological and Environmental Research under Contract No. DE-AC02-05CH11231. Constructive comments of four anonymous reviewers improved the quality of the manuscript.

## Research Data

All data used in this study are accessible on the ESS-DIVE database (<https://ess-dive.lbl.gov>).

## Appendix A. Supplementary material

Supplementary material to this article can be found online at <https://doi.org/10.1016/j.gca.2022.11.002>.

## References

- Ahmadi, N., Acocella, M., Fries, E., Mosthaf, K., Rolle, M., 2022. Oxygen propagation fronts in porous media under evaporative conditions at the soil/atmosphere interface: Lab-scale experiments and model-based interpretation. *Water Resour. Res.* 58, 1–20.
- Ameli, A., Beven, K., Erlandsson, M., Creed, I., McDonnell, J., Bishop, K., 2017. Primary weathering rates, water transit times, and concentration-discharge relations: a theoretical analysis for the critical zone. *Water Resour. Res.* 53, 942–960.
- Amiotte-Suchet, P., Probst, J., Ludwig, W., 2003. Worldwide distribution of continental rock lithology: implications for the atmospheric/soil CO<sub>2</sub> uptake by continental weathering and alkalinity river transport to the oceans. *Global Biogeochem. Cycles* 17, 1038–1051.
- Arora, B., Spycher, N., Steefel, C., Molins, S., Bill, M., Conrad, M., Dong, W., Faybishenko, B., Tokunaga, T.K., Wan, J., Williams, K.H., Yabusaki, S., 2016. Influence of hydrological, biogeochemical and temperature transients on subsurface carbon fluxes in a flood plain environment. *Biogeochem.* 127, 367–396.
- Arora, B., Burrus, M., Newcomer, M., Steefel, C., Carroll, R., Dwivedi, D., Dong, W., Williams, K., Hubbard, S., 2021. Differential C-Q analysis: a new approach to inferring lateral transport and hydrologic transients within multiple reaches of a mountainous headwater catchment. *Front. Water* 2 (24), 1–20.
- Bao, Z., Haberer, C., Maier, U., Amos, R., Blowes, D., Grathwohl, P., 2017. Modeling controls on the chemical weathering of marine mudrocks from the Middle Jurassic in Southern Germany. *Chem. Geol.* 459, 1–12.
- Battistel, M., Muniruzzaman, M., Onses, F., Lee, J., Rolle, M., 2019. Reactive fronts in chemically heterogeneous porous media: experimental and modeling investigation of pyrite oxidation. *Appl. Geochem.* 100, 77–89.
- Battistel, M., Stolze, L., Muniruzzaman, M., Rolle, M., 2021. Arsenic release and transport during oxidative dissolution of spatially-distributed sulfide minerals. *J. Hazard. Mat.* 409, 124651.
- Beaulieu, E., Godd eris, Y., Labat, D., Roelandt, C., Calmels, D., Gaillardet, J., 2011. Modeling of water-rock interaction in the Mackenzie basin: Competition between sulfuric and carbonic acids. *Chem. Geol.* 289 (1–2), 114–123.
- Bibi, I., Singh, B., Silvester, E., 2011. Dissolution of illite in saline-acidic solutions at 25°C. *Geochim. Cosmochim. Acta* 75, 3237–3249.
- Blanc, P., Lassin, A., Piantone, P., Azaroual, M., Jacquemet, N., Fabbri, A., Gaucher, E., 2012. Thermodynam: a geochemical database focused on low temperature water/rock interactions and waste materials. *Appl. Geochem.* 27, 2107–2116.
- Bolton, E., Berner, R., Petsch, S., 2006. The weathering of sedimentary organic matter as a control on atmospheric O<sub>2</sub>: II. Theoretical modeling. *Am. J. Sci.* 306, 575–615.
- Brandt, F., Bosbach, D., Krawczyk-B arsch, E., Arnold, T., Bernhard, G., 2003. Chlorite dissolution in the acid pH-range: a combined microscopic and macroscopic approach. *Geochim. Cosmochim. Acta* 67 (8), 1451–1461.
- Carrier, W., 2003. Goodbye, Hazen; Hello, Kozeny-Carman. *J. Geotech. Geoenviron. Eng.*
- Carroll, R., Bearup, L., Brown, W., Dong, W., Bill, M., Williams, K., 2018. Factors controlling seasonal groundwater and solute flux from snow-dominated basins. *Water Critic. Zone* 32, 2187–2202.
- Chapelle, F., 2021. The bioavailability of dissolved, particulate, and adsorbed organic carbon in groundwater systems. *Groundwater* 59 (2), 226–235.
- Cogorno, J., Stolze, L., Muniruzzaman, M., Rolle, M., 2022. Dimensionality effects on multicomponent ionic transport and surface complexation in porous media. *Geochim. Cosmochim. Acta* 318, 230–246.
- Copard, Y., Amiotte-Suchet, P., Di-Giovanni, C., 2007. Storage and release of fossil organic carbon related to weathering of sedimentary rocks. *Earth Planet. Sci. Lett.* 258, 345–357.
- Dere, A., White, T., April, R., Reynolds, B., Miller, T., Knapp, E., McKay, L.D., Brantley, S., 2013. Climate dependence of feldspar weathering in shale soils along a latitudinal gradient. *Geochim. Cosmochim. Acta* 122 (101–126).
- Dwivedi, D., Riley, W., Torn, M., Spycher, N., Maggi, F., Tang, J., 2017. Mineral properties, microbes, transport, and plant-input profiles control vertical distribution and age of soil carbon stocks. *Soil Biol. Biochem.* 107, 244–259.
- Dwivedi, D., Steefel, C., Arora, B., Newcomer, M., Moulton, J., Dafflon, B., Faybishenko, B., Fox, P., Nico, P., Spycher, N., Carroll, R., Williams, K., 2018a. Geochemical exports to river from the intrameander hyporheic zone under transient hydrologic conditions: East River Mountainous Watershed, Colorado. *Water Resour. Res.* 54, 8456–8477.
- Dwivedi, D., Arora, B., Steefel, C., Dafflon, B., Versteeg, R., 2018b. Hot spots and hot moments of nitrogen in a riparian corridor. *Water Resour. Res.* 54, 205–222.
- Dwivedi, D., Tang, J., Bouskill, N., Georgiou, K., Chacon, S., Riley, W., 2019. Abiotic and biotic controls and soil organic-mineral interactions: developing model structures to analyze why soil organic matter persists. *Rev. Min. Geochem.* 85, 329–348.
- Dwivedi, D., Mital, U., Faybishenko, B., Dafflon, B., Varadharajan, C., Agarwal, D., Williams, K.H., Steefel, C., Hubbard, S., 2022. Imputation of contiguous gaps and extremes of subhourly groundwater time series using random forests. *J. Mach. Learn. Model. Comput.* 3 (2), 1–22.
- Eberl, D., 2003. User's guide to RockJock—A program for determining quantitative mineralogy from powder X-ray diffraction data. Revised 11/30/09. U.S. Geological Survey Open File Report 03–78, 1–48.
- Fox, P., Bill, M., Heckman, K., Conrad, M., Anderson, C., Keiluweit, M., Nico, P., 2020. Shale as a source of organic carbon in floodplain sediments of a mountainous watershed. *J. Geophys. Res.* 125 (2), 1–21.
- Fox, P., Carrero, S., Anderson, C., Dewey, C., Keiluweit, M., Conrad, M., Naughton, H., Fendorf, S., Carroll, R., Dafflon, B., Malenda-Lawrence, H., Dwivedi, D., Gilbert, B., Christensen, J., Boye, K., Beutler, C., Brown, W., Newman, A., Versteeg, R., Williams, K., Nico, P., 2022. Sulfur biogeochemical cycling and redox dynamics in a shale-dominated mountainous watershed. *J. Geophys. Res. Biogeosci.* 127, 1–18.
- Gaste-Rector, S., Blanton, T., 2019. The Powder Diffraction File: A quality materials characterization database. *Powder Diff.* 34, 352–360.
- Godderis, Y., Francois, L., Probst, A., Schott, J., Moncoulon, D., Labat, D., Viville, D., 2006. Modelling weathering processes at the catchment scale: the WITCH numerical model. *Geochim. Cosmochim. Acta* 70, 1128–1147.
- Gu, X., Rempe, D., Dietrich, W., West, A., Lin, T., Jin, L., Brantley, S., 2020a. Chemical reactions, porosity and microfracturing in shale during weathering: the effect of erosion rate. *Geochim. Cosmochim. Acta* 269, 63–100.
- Gu, X., Mavko, G., Ma, L., Oakley, D., Accardo, N., Carr, B., Nyblade, A., Brantley, S., 2020b. Seismic refraction tracks porosity generation and possible CO<sub>2</sub> production at depth under a headwater catchment. *PNAS* 117 (32), 18991–18997.
- Haberer, C., Muniruzzaman, M., Grathwohl, P., Rolle, M., 2015. Diffusive-dispersive fronts in porous media: iron(II) oxidation at the unsaturated-saturated interface. *Vadose Zone J.*, 1–14.
- Heidari, P., Li, L., Jin, L., Williams, J., Brantley, S., 2017. A reactive transport model for Marcellus shale weathering. *Geochim. Cosmochim. Acta* 217, 421–440.
- Helgeson, H., Delany, J., Nesbitt, H., Bird, D., 1978. Summary and critique of the thermodynamic properties of rock-forming minerals. *Am. J. Sci.* 278-A, 1–229.
- Helgeson, H., Murphy, W., Aagaard, P., 1984. Thermodynamic and kinetic constraints on reaction rates among minerals and aqueous solutions. II. Rate constants, effective surface area, and the hydrolysis of feldspar. *Geochim. Cosmochim. Acta* 48 (12), 2405–2432.
- Houlton, B., Morford, S., Dahlgren, R., 2018. Convergent evidence for widespread rock nitrogen sources in Earth's surface environment. *Sci.* 360, 58–62.
- Hubbard, S., Williams, K., Agarwal, D., Banfield, J., Beller, H., Bouskill, N., Brodie, E., Carroll, R., Dafflon, B., Dwivedi, D., Falco, N., Faybishenko, B., Maxwell, R., Nico, P., Steefel, C., Steltzer, H., Tokunaga, T., Tran, P.A., Wainwright, H., 2018. The East River, Colorado, Watershed: a mountainous community testbed for improving predictive understanding of multiscale hydrological-biogeochemical dynamics. *Vadose Zone J.* 17 (180061), 1–25.
- Hunt, A., Egli, M., Faybishenko, B., 2021. Hydrogeology, chemical weathering, and soil formation. *American Geophysical Union*.
- Jardine, P., Sanford, W., Gwo, J., Reedy, O., Hicks, D., Riggs, J., Bailey, W., 1999. Quantifying diffusive mass transfer in fractured shale bedrock. *Water Resour. Res.* 35 (7), 2015–2030.
- Jin, L., Mathur, R., Rother, G., Cole, D., Bazilevskaya, E., Williams, J., Carone, A., Brantley, S., 2013. Evolution of porosity and geochemistry in Marcellus Formation black shale during weathering. *Chem. Geol.* 356, 50–63.
- Jin, L., Ogrinc, N., Yeasavage, T., Ea, H., Ma, L., Sullivan, P., Kaye, J., Duffy, C., Brantley, S., 2014. The CO<sub>2</sub> consumption potential during gray shale weathering: insights from the evolution of carbon isotopes in the Susquehanna Shale Hills critical zone observatory. *Geochim. Cosmochim. Acta* 142, 260–280.
- Jin, L., Rother, G., Cole, D., Mildner, D., Duffy, C., Brantley, S., 2011. Characterization of deep weathering and nanoporosity development in shale - a neutron study. *Am. Min.* 96, 498–512.
- K hler, S., Dufaud, F., Oelkers, E., 2003. An experimental study of illite dissolution kinetics as a function of pH from 1.4 to 12.4 and temperature from 5 to 50°C. *Geochim. Cosmochim. Acta* 67 (19), 3583–3594.
- Lasaga, A., 1984. Chemical kinetics of water-rock interactions. *J. Geophys. Res.* 89 (86), 4009–4025.
- Lasaga, A., 1998. Kinetic theory in the Earth Sciences. Princeton University Press, Princeton.
- Lebedeva, M., Brantley, S., 2020. Relating the depth of the water table to the depth of weathering. *Earth Surf. Process. Landforms* 45, 2167–2178.
- Li, L., Maher, K., Navarre-Sitchler, A., Druhan, J., Meile, C., Lawrence, C., Moore, J., Perdrial, J., Sullivan, P., Thompson, A., Jin, L., Bolton, E.W., Brantley, S., Dietrich, W.E., Mayer, K., Steefel, C., Valocchi, A., Zachara, J., Kocar, B., McIntosh, J., Tutolo, B., Kumar, M., Sonnenthal, E., Bao, C., Beisman, J., 2017. Expanding the role of reactive transport models in critical zone processes. *Earth-Sci. Rev.* 165, 280–301.
- Li, Z.,  zgen-Xian, I., Maina, F., 2021. A mass-conservative predictor-corrector solution to the 1D Richards equation with adaptive time control. *J. Hydrol.* 592, 1–16.
- Litke, R., Klussman, U., Krooss, B., Leythaeuser, D., 1991. Quantification of loss of calcite, pyrite, and organic matter due to the weathering of Toarcian black shales and effects of kerogen and bitumen characteristics. *Geochim. Cosmochim. Acta* 55, 3369–3378.
- Ma, L., Jin, L., Brantley, S., 2011. How mineralogy and slope aspect affect REE release and fractionation during shale weathering in the Susquehanna/Shale Hills Critical Zone Observatory. *Chem. Geol.* 290, 31–49.

- Maher, K., 2011. The role of fluid residence time and topographic scales in determining chemical fluxes from landscapes. *Earth Planet. Sci. Lett.* 312, 48–58.
- Maher, K., Navarre-Sitchler, A., 2019. Reactive transport processes that drive chemical weathering: from making space for water to dismantling continents. *Rev. Min. Geochem.* 85, 349–380.
- Maher, K., Steefel, C., White, A., Stonestrom, D., 2009. The role of reaction affinity and secondary minerals in regulating chemical weathering rates at the Santa Cruz Soil Chronosequence, California. *Geochim. Cosmochim. Acta* 73, 2804–2831.
- Majzlan, J., Grevel, K.-D., Navrotsky, A., 2003. Thermodynamics of iron oxides. H. Enthalpies of formation and relative stability of goethite ( $\alpha$ -FeOOH), lepidocrocite ( $\gamma$ -FeOOH), and maghemite ( $\gamma$ -Fe<sub>2</sub>O<sub>3</sub>). *Am. Min.* 88, 855–859.
- Manning, A., Verplanck, P., Caine, J., Todd, A., 2013. Links between climate change, water-table depth, and water chemistry in a mineralized mountain watershed. *Appl. Geochem.* 37, 64–78.
- Marouf, R., Marouf-Khelifa, K., Schott, J., Khelifa, A., 2009. Zeta potential study of thermally treated dolomite samples in electrolyte solutions. *Micropor. Mesopor. Mat.* 122, 99–104.
- McKibben, M., Barnes, H., 1986. Oxidation of pyrite in low temperature acidic solutions: rate laws and surface textures. *Geochim. Cosmochim. Acta* 50, 1509–1520.
- Meurer, K., Barron, J., Chenu, C., Coucheney, E., Fielding, M., Hallet, P., Herrmann, A. M., Keller, T., Koestel, J., Larsbo, M., Lewan, E., Or, D., Parsons, D., Parvin, N., Taylor, A., Vereecken, H., Jarvis, N., 2020. A framework for modelling soil structure dynamics induced by biological activity. *Glob. Change Biol.* 26, 5382–5403.
- Millington, R., Quirk, J., 1961. Permeability of porous solids. *Trans. Faraday Soc.* 57, 1200–1207.
- Moore, O., Buss, H., Dosseto, A., 2019. Incipient chemical weathering at bedrock fracture interfaces in a tropical critical zone system, Puerto Rico. *Geochim. Cosmochim. Acta* 252, 61–87.
- Morrison, S., Goodknight, C., Tigar, A., Bush, R., Gil, O., 2012. Naturally occurring contamination in the Mancos Shale. *Environ. Sci. Technol.* 46, 1379–1387.
- Moses, C., Nordstrom, D., Herman, J., Mills, A., 1987. Aqueous pyrite oxidation by dissolved oxygen and by ferric iron. *Geochim. Cosmochim. Acta* 51, 1561–1571.
- Mualem, Y., 1976. A new model for predicting the hydraulic conductivity of unsaturated porous media. *Water Resour. Res.* 12, 513–522.
- Muniruzzaman, M., Karlsson, T., Ahmadi, N., Kauppila, P., Kauppila, T., Rolle, M., 2021. Weathering of unsaturated waste rocks from Kevisa and Hitura mines: pilot-scale lysimeter experiments and reactive transport modeling. *Appl. Geochem.* 130 (104984).
- Navarre-Sitchler, A., Steefel, C., Sak, P., Brantley, S., 2011. A reactive transport model for weathering rind formation on basalt. *Geochim. Cosmochim. Acta* 75, 7644–7667.
- Navarre-Sitchler, A., Brantley, S., Rother, G., 2015. How porosity increases during incipient weathering of crystalline silicate rocks. *Rev. Min. Geochem.* 80, 331–354.
- Newcomer, M., Bouskill, N., Wainwright, H., Maavara, T., Arora, B., Siirila-Woodburn, E., Dwivedi, D., Williams, K., Steefel, C., Hubbard, S., 2021. Hysteresis patterns of watershed nitrogen retention and loss over the past 50 years in United States hydrological basins. *Global Biogeochem. Cycles* 35, 1–28.
- Palandri, J., Kharaka, Y., 2004. A compilation of rate parameters of water-mineral interaction kinetics for application to geochemical modeling. *US Geological Survey, Open file report 2004-1068*, 1–70.
- Pandey, S., Rajaram, H., 2016. Modeling the influence of preferential flow on the spatial variability and time-dependence of mineral weathering rates. *Water Resour. Res.* 52, 9344–9366.
- Petsch, S., Berner, R., Eglinton, T., 2000. A field study of the chemical weathering of ancient sedimentary organic matter. *Org. Geochem.* 31, 475–487.
- Petsch, S., Edwards, K., Eglinton, T., 2005. Microbial transformations of organic matter in black shales and implications for global biogeochemical cycles. *Palaeo.* 219, 157–170.
- Putz, H., Branderburg, K., 2011. Match! - Phase identification from powder diffraction. *Crystal Impact* 3 (8), 137.
- Quirk, B., Huss, E., Laabs, B., Leonard, E., Licciardi, J., Plummer, M., Caffee, M., 2022. Late Pleistocene glacial chronologies and paleoclimate in the northern Rocky mountains. *Clim. Past* 18, 293–312.
- Regnier, P., Steefel, C., 1999. A high resolution estimate of the inorganic nitrogen flux from the Scheldt estuary to the coastal North Sea during a nitrogen-limited algal bloom, spring 1995. *Geochim. Cosmochim. Acta* 63 (9), 1359–1374.
- Richert, P., Bottinga, Y., Denielon, L., Petitet, J., Tequi, C., 1982. Thermodynamics properties of quartz, cristobalite and amorphous SiO<sub>2</sub>: Drop calorimetry measurements between 1000 and 1800 K and a review from 0 to 2000 K. *Geochim. Cosmochim. Acta* 46, 2639–2658.
- Robie, R., Hemingway, B., 1995. Thermodynamic properties of minerals and related substances at 298.15 K and 1 Bar (105 Pascals) pressure and at higher temperatures. *U.S. Geol. Survey Bull.* 2131, 461.
- Rogers, D., Newcomer, M., Raberg, J., Dwivedi, D., Steefel, C., Bouskill, N., Nico, P., Faybishenko, B., Fox, P., Conrad, M., Bill, M., Brodie, E., Arora, B., Dafflon, B., Williams, K.H., Hubbard, S., 2021. Modeling the impact of riparian hollows on river corridor nitrogen exports. *Front. Water* 3, 1–18.
- Schillawski, S., Petsch, S., 2008. Release of biodegradable dissolved organic matter from ancient sedimentary rocks. *Glob. Biogeochem. Cycles* 22, 1–8.
- Seigneur, N., Mayer, K., Steefel, C., 2019. Reactive transport in evolving porous media. *Rev. Miner. Geochem.* 85 (1), 197–238.
- Singer, P., Stumm, W., 1970. Acidic mine drainage: the rate-determining step. *Sci.* 167 (3921), 1121–1123.
- Sø, H., Postma, D., Jakobsen, R., Larsen, F., 2012. Competitive adsorption of arsenate and phosphate onto calcite; experimental results and modeling with CCM and CD-MUSIC. *Geochim. Cosmochim. Acta* 93, 1–13.
- Sorensen, P., Beller, H., Bill, M., Bouskill, N., Hubbard, S., Karaoz, U., Polussa, A., Steltzer, H., Wang, S., Williams, K.H., Wu, Y., Brodie, E., 2020. The snowmelt niche differentiates three microbial life strategies that influence soil nitrogen availability during and after winter. *Front. Microbiol.* 11 (871), 1–18.
- Steefel, C., 2019. Reactive transport at the crossroads. *Rev. Min. Geochem.* 85, 1–26.
- Steefel, C., Lasaga, A., 1994. A coupled model for transport of multiple chemical species and kinetic precipitation/dissolution reactions with application to reactive flow in single phase hydrothermal systems. *Am. J. Sci.* 294, 529–592.
- Steefel, C., MacQuarrie, K., 1996. Approaches to modeling reactive transport in porous media. In: Lichtner, P., Steefel, C., Oelkers, E. (Eds.), *Reactive Transport in Porous Media, Reviews in Mineralogy* 34. Mineralogy Society of America, pp. 83–129.
- Steefel, C., Yabusaki, S., 1996. OS3D/GIMRT, Software for multicomponent-multidimensional reactive transport. In *User manual and programmer's guide* (PNL-11166). Pacific North-West National Laboratory, Richland, Washington.
- Steefel, C., DePaolo, D., Lichtner, P., 2005. Reactive transport modeling: an essential tool and a new research approach for the Earth sciences. *Earth Planet. Sci. Lett.* 240 (3–4), 539–558.
- Steefel, C., Appelo, C., Arora, B., Jacques, D., Kalbacher, T., Kolditz, O., Lagneau, V., Lichtner, P.C., Mayer, K.U., Meeussen, J.C.L., Molins, S., Moulton, D., Shao, H., Simunek, J., Spycher, N., Yabusaki, S.B., Yeh, G., 2015. Reactive transport codes for subsurface environmental simulation. *Comput. Geosci.* 19, 445–478.
- Stewart, B., Shanley, J., Kirchner, J., Norris, D., Adler, T., Bristol, B., Harpold, A.A., Perdrial, J.N., Rizzo, D.M., Sterle, G., Underwood, K.L., Wen, H., Li, L., 2021. Streams as mirrors: reading subsurface water chemistry from stream chemistry. *Water Resour. Res.* 58, 1–20.
- Stolze, L., Zhang, D., Guo, H., Rolle, M., 2019a. Model-based interpretation of groundwater arsenic mobility during in situ reductive transformation of ferrihydrite. *Environ. Sci. Technol.* 53, 6845–6854.
- Stolze, L., Zhang, D., Guo, H., Rolle, M., 2019b. Surface complexation modeling of arsenic mobilization from goethite: interpretation of an in-situ experiment. *Geochim. Cosmochim. Acta* 248, 274–288.
- Stolze, L., Wagner, J., Damsgaard, C., Rolle, M., 2020. Impact of surface complexation and electrostatic interactions on pH front propagation in silica porous media. *Geochim. Cosmochim. Acta* 277, 132–149.
- Stolze, L., Battistel, M., Rolle, M., 2022. Oxidative dissolution of arsenic-bearing sulfide minerals in groundwater: impact of hydrochemical and hydrodynamic conditions on arsenic release and surface evolution. *Environ. Sci. Technol.* 56 (8), 5049–5061.
- Stumm, W., Morgan, J., 1961. Oxygenation of ferrous iron. *Ind. Eng. Chem.* 53, 143–146.
- Szramke, K., McIntosh, J., Williams, E., Kanduc, T., Ogrinc, N., Walter, L., 2007. Relative weathering intensity of calcite versus dolomite in carbonate-bearing temperate zone watersheds: carbonate geochemistry and fluxes from catchments within the St. Lawrence and Danube river basins. *Geochim. Geophys. Geosys.* 8 (4), 1–26.
- Tokunaga, T., Wan, J., Williams, K., Brown, W., Henderson, A., Kim, Y., Tran, A.P., Conrad, M.E., Bill, M., Carroll, R.W.H., Dong, W., Xu, Z., Lavy, A., Gilbert, B., Carrero, S., Christensen, J.N., Faybishenko, B., Arora, B., Siirila-Woodburn, E., 2019. Depth- and time-resolved distributions of snowmelt-driven hillslope subsurface flow and transport and their contributions to surface waters. *Water Resour. Res.* 55, 9474–9499.
- Tremosa, J., Debure, M., Narayanasamy, S., Redon, P., Jacques, D., Claret, F., Robinet, J., 2020. Shale weathering: a lysimeter and modelling study for flow, transport, gas diffusion an reactivity assessment in the critical zone. *J. Hydrol.* 587, 124925.
- Tuttle, M., Breit, G., Goldhaber, M., 2009. Weathering of the New Albany Shale, Kentucky: II. Redistribution of minor and trace elements. *Appl. Geochem.* 24, 1565–1578.
- Van Capellen, P., Gaillard, J., 1996. Chapter 8. Biogeochemical dynamics in aquatic sediments. *Reactive transport in porous media*. Walter de Gruyter GmbH, Berlin/Munich/Boston.
- Van Capellen, P., Wang, Y., 1995. Metal cycling in surface sediments: Modeling the interplay of transport and reaction. In: Allen, H. (Ed.), *Metal contaminated sediments*. Ann Arbor Press, Chelsea, pp. 21–64.
- van Genuchten, M., 1980. A closed-formulation for predicting the hydraulic conductivity of unsaturated soils. *Soil Sci. Soc. Am. J.* 44, 892–898.
- Wan, J., Tokunaga, T., Williams, K., Dong, W., Brown, W., Henderson, A., Newman, A. W., Hubbard, S., 2019. Predicting sedimentary bedrock subsurface weathering fronts and weathering rates. *Nat. Sci. Rep.* 9 (17198).
- Wan, J., Tokunaga, T., Brown, W., Newman, A., Dong, W., Bill, M., Beutler, C.A., Henderson, A.N., Harvey-Costello, N., Conrad, M.E., Bouskill, N.J., Hubbard, S.S., Williams, K., 2021. Bedrock weathering contributes to subsurface reactive nitrogen and nitrous oxide emissions. *Nat. Geo.* 14, 217–224.
- White, A., Schulz, M., Stonestrom, D., Vivit, D., Fitzpatrick, J., Bullen, T., Maher, K., Blum, A., 2009. Chemical weathering of a marine terrace chronosequence, Santa Cruz, California. Part II: Solute profiles, gradients and the comparisons of contemporary and long-term weathering rates. *Geochim. Cosmochim. Acta* 73, 2769–2803.

- Wildman, R., Berner, R., Petsch, S., Bolton, E., Eckert, J., Mok, U., Evans, B., 2004. The weathering of sedimentary organic matter as a control on atmospheric O<sub>2</sub>: I. Analysis of a black shale. *Am. J. Sci.* 304, 239–249.
- Williamson, M., Rimstidt, J., 1994. The kinetics and electrochemical rate-determining step of aqueous pyrite oxidation. *Geochim. Cosmochim. Acta* 58, 5443–5454.
- Winnick, M., Carroll, R., Williams, K., Maxwell, R., Dong, W., Maher, K., 2017. Snowmelt controls on concentration-discharge relationships and the balance of oxidative and acid-base weathering fluxes in an alpine catchment, East River, Colorado. *Water Resour. Res.* 53, 2507–2523.
- Yabusaki, S., Wilkins, M., Fang, Y., Williams, K., Arora, B., Bargar, J., Beller, H., Bouskill, N., Brodie, E., Christensen, J., Conrad, M., Danczak, R., King, E., Soltanian, M., Spycher, N., Steefel, C., Tokunaga, T., Versteeg, R., 2017. Water table dynamics and biogeochemical cycling in a shallow, variably-saturated floodplain. *Environ. Sci. Technol.* 51, 3307–3317.
- Zhou, Q., Liu, H., Molz, F., Zhang, Y., Bodvarsson, G., 2007. Field-scale effective matrix diffusion coefficient for fractured rock: results from literature survey. *J. Contam. Hydrol.* 93, 161–187.